Article

Cell Reports

KRAS Engages AGO2 to Enhance Cellular Transformation

Graphical Abstract

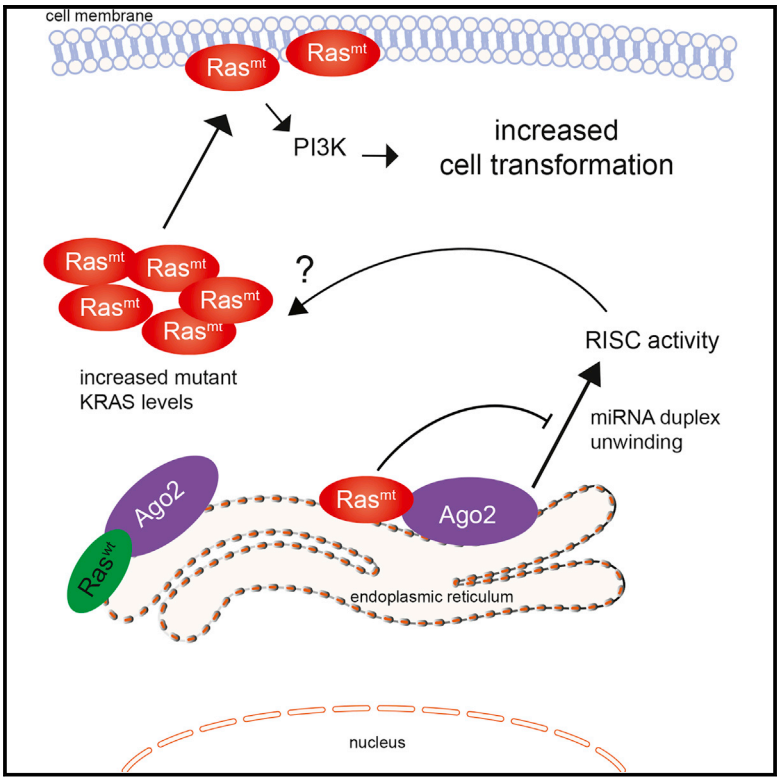

Highlights

- RAS interacts with AGO2 in the membrane component of the endoplasmic reticulum
- The N terminus of AGO2 directly binds the Switch II domain of RAS
- Oncogenic KRAS association inhibits AGO2-mediated microRNA duplex unwinding
- AGO2 interaction elevates oncogenic KRAS levels to enhance cellular transformation

Authors

Sunita Shankar, Sethuramasundaram Pitchiaya, Rohit Malik, ..., Nils G. Walter, Chandan Kumar-Sinha, Arul M. Chinnaiyan

Correspondence

arul@umich.edu

In Brief

Shankar et al. show that RAS interacts with AGO2, a key component of the RNA-silencing machinery. Interaction of oncogenic KRAS with AGO2 in the endoplasmic reticulum inhibits AGO2 function, elevates mutant KRAS protein levels, and enhances cellular transformation. AGO2 is required for maximal KRAS-mediated oncogenesis.

Shankar et al., 2016, Cell Reports *14*, 1448–1461
February 16, 2016
http://dx.doi.org/10.1016/j.celrep.2016.01.034

CellPress

OPEN ACCESS
CellPress

Cell Reports
Article

KRAS Engages AGO2 to Enhance Cellular Transformation

Sunita Shankar,[1,2] Sethuramasundaram Pitchiaya,[1,2,3] Rohit Malik,[1,2] Vishal Kothari,[1,2] Yasuyuki Hosono,[1,2] Anastasia K. Yocum,[1,2] Harika Gundlapalli,[1,2] Yasmine White,[4] Ari Firestone,[4] Xuhong Cao,[1,5] Saravana M. Dhanasekaran,[1,2] Jeanne A. Stuckey,[6,7] Gideon Bollag,[8] Kevin Shannon,[4] Nils G. Walter,[3] Chandan Kumar-Sinha,[1,2] and Arul M. Chinnaiyan[1,2,5,9,10,*]

[1]Michigan Center for Translational Pathology, University of Michigan, Ann Arbor, MI 48109, USA
[2]Department of Pathology, University of Michigan, Ann Arbor, MI 48109, USA
[3]Single Molecule Analysis Group, Department of Chemistry, University of Michigan, Ann Arbor, MI 48109, USA
[4]Department of Pediatrics and Helen Diller Family Comprehensive Cancer Center, University of California, San Francisco, San Francisco, CA 94158, USA
[5]Howard Hughes Medical Institute, University of Michigan, Ann Arbor, MI 48109, USA
[6]Life Science Institute, University of Michigan, Ann Arbor, MI 48109, USA
[7]Department of Biological Chemistry, University of Michigan, Ann Arbor, MI 48109, USA
[8]Plexxikon Inc., Berkeley, CA 94710, USA
[9]Comprehensive Cancer Center, University of Michigan, Ann Arbor, MI 48109, USA
[10]Department of Urology, University of Michigan, Ann Arbor, MI 48109, USA
*Correspondence: arul@umich.edu
http://dx.doi.org/10.1016/j.celrep.2016.01.034

SUMMARY

Oncogenic mutations in RAS provide a compelling yet intractable therapeutic target. Using co-immunoprecipitation mass spectrometry, we uncovered an interaction between RAS and Argonaute 2 (AGO2). Endogenously, RAS and AGO2 co-sediment and co-localize in the endoplasmic reticulum. The AGO2 N-terminal domain directly binds the Switch II region of KRAS, agnostic of nucleotide (GDP/GTP) binding. Functionally, AGO2 knockdown attenuates cell proliferation in mutant *KRAS*-dependent cells and *AGO2* overexpression enhances $KRAS^{G12V}$-mediated transformation. Using *AGO2*−/− cells, we demonstrate that the RAS-AGO2 interaction is required for maximal mutant KRAS expression and cellular transformation. Mechanistically, oncogenic KRAS attenuates AGO2-mediated gene silencing. Overall, the functional interaction with AGO2 extends KRAS function beyond its canonical role in signaling.

INTRODUCTION

Approximately one-third of human cancers harbor an oncogenic mutation in *HRAS*, *KRAS*, or *NRAS* (Balmain and Pragnell, 1983; Karnoub and Weinberg, 2008; Pylayeva-Gupta et al., 2011). The tumor types most frequently harboring *RAS* mutations, predominantly in *KRAS*, include pancreatic, lung, and colon carcinoma, among others (COSMIC, 2013; Hand et al., 1984; Karachaliou et al., 2013; Lauchle et al., 2006; Löhr et al., 2005). *RAS* genes encode a family of small GTPases (Sweet et al., 1984) that transduce extracellular growth signals by cycling between an active GTP-bound state and an inactive GDP-bound state (Karnoub and Weinberg, 2008; Schubbert et al., 2007). Oncogenic Ras proteins exhibit reduced intrinsic GTPase activity and are resistant to negative regulation by GTPase-activating proteins (GAPs) such as p120GAP and neurofibromin (Cichowski and Jacks, 2001). Constitutively elevated levels of Ras-GTP aberrantly activate downstream effector pathways that promote neoplastic transformation (Karnoub and Weinberg, 2008; Shaw and Cantley, 2006; Trahey and McCormick, 1987). Despite extensive characterization of the Ras/GAP molecular switch(es) and downstream signaling axes, therapeutic targeting of RAS-driven cancers remains elusive (Baines et al., 2011; Downward, 2003; Stephen et al., 2014).

The oncogenic activity of RAS-GTP is mediated through canonical effectors including RAF, PI3 kinase (PI3K), and RalGDS (Cox and Der, 2010; Karnoub and Weinberg, 2008), and other effectors have been described in various contexts (Gysin et al., 2011). RAS effectors bind through the conserved Switch I and Switch II domains and drive cellular transformation by activating downstream kinases and GTPase-signaling modules, the best known of which are the RAF/MEK/ERK (mitogen activation protein [MAP] kinase) and the PI3K/Akt signaling cascades. RAS interactors have been identified using conventional approaches of ectopically expressed epitope-tagged *RAS* constructs (Goldfinger et al., 2007; Vasilescu et al., 2004). Here, we employed co-immunoprecipitation followed by mass spectrometry (coIP MS) to analyze the endogenous interactome of RAS in a panel of lung and pancreatic cancer cell lines representing the spectrum of both *KRAS* mutation and dependency status. Surprisingly, the most prominent interacting protein, across all cell lines analyzed,

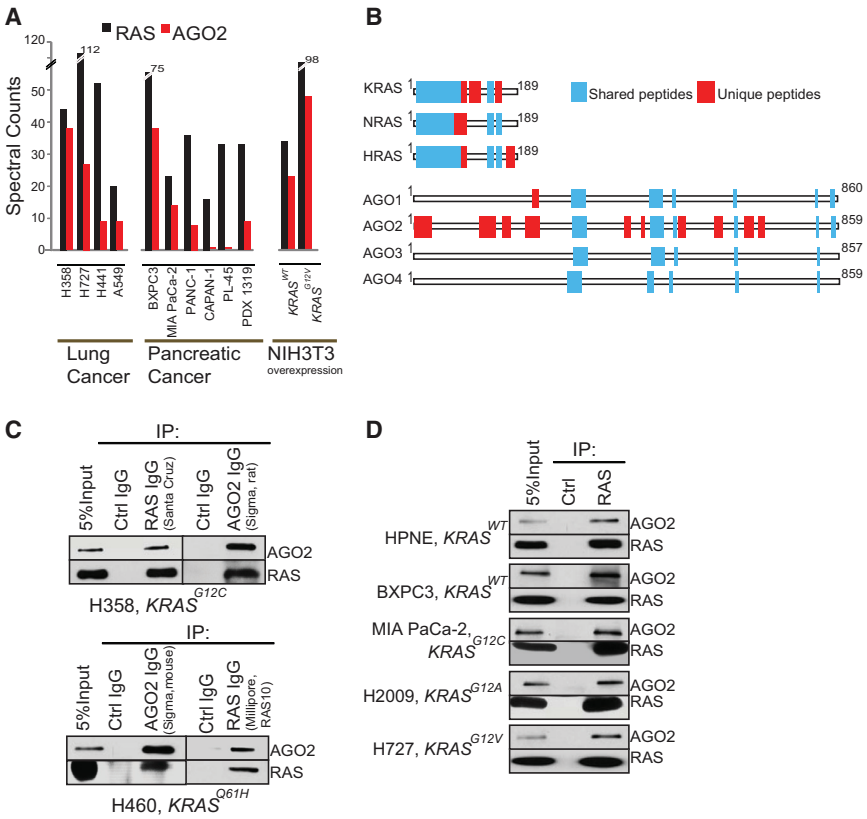

Figure 1. Identification of the RAS-AGO2 Interaction

(A) Spectral counts of RAS and AGO2 peptides detected in RAS co-immunoprecipitation mass spectrometric (coIP MS) analysis in the indicated cancer cell lines and NIH3T3 cells expressing $KRAS^{WT}$ and $KRAS^{G12V}$.

(B) Distribution of peptides mapping to RAS and AGO gene families from RAS coIP MS based on ClustalW alignments. Representative experiment from H358 cells is shown. Blue boxes indicate peptides mapping to multiple gene family members, and red boxes indicate peptides mapping uniquely to a protein.

(C) Immunoprecipitation (IP) of RAS or AGO2 in H358 (left) and H460 (right) lung cancer cells followed by immunoblot analysis using multiple distinct antibodies, as indicated.

(D) IP of RAS from a panel of benign and cancer cells with differing mutational status of *KRAS* (as indicated) followed by immunoblot analysis of AGO2 or RAS. RAS10 mAb was used for IB.

See also Figure S1.

was EIF2C2, commonly known as Argonaute 2 (AGO2), a key effector of the RNA-silencing pathway. Interestingly, a role for AGO2 in RAS-induced senescence has been described recently (Benhamed et al., 2012; Yang et al., 2014). Also, phosphorylation of AGO2 by MAPK/PI3K pathway activators has been shown to alter its microRNA-related function through different mechanisms (Horman et al., 2013; Rüdel et al., 2011; Shen et al., 2013; Zeng et al., 2008), portending a broader, direct interface between intracellular signaling and RNA-silencing mechanisms (Paroo et al., 2009). Considering the potential functional implications of RAS-AGO2 interaction, here we corroborated and characterized this interaction in detail.

RESULTS

Endogenous RAS and AGO2 Interaction

To analyze RAS-interacting proteins in an endogenous setting, we first used the pan-RAS antibody RAS10 (Cheng et al., 2011), which efficiently immunoprecipitates RAS proteins by binding to the Switch I domain (amino acids [aa] 32–40; Figures S1A–S1C). Co-immunoprecipitation of RAS followed by tandem mass spectrometry (RAS coIP MS) was performed as outlined in Figure S1D using a panel of ten lung and pancreatic cancer cell lines of known *KRAS* mutation status (Table S1), as well as NIH 3T3 cells ectopically overexpressing human *KRAS* wild-type ($KRAS^{WT}$) or mutant ($KRAS^{G12V}$) proteins. Peptide fragments deduced from MS analyses spectral counts revealed robust detection of the bait protein (RAS) in all the 12 cell lines, as expected (Table S2). To minimize individual cell-specific observations in the endogenous system employed, we focused on observations common across different cell lines. Intriguingly, peptides spanning EIF2C2 protein, commonly known as AGO2, the catalytic component of the RNA-induced silencing complex (RISC), were observed in the RAS coIP MS of all cancer cell lines (n = 10) tested, as well as in NIH 3T3 cells expressing $KRAS^{WT}$ or $KRAS^{G12V}$ (Figure 1A). Remarkably, only the RAS and AGO2 peptides were detected in every cell line tested, with cumulative spectral counts of 576 and 229, respectively. Other interactors detected in five or more of the 12 cell lines are tabulated in Table S2. The significant lack of peptides spanning the RAS effectors like RAF/PI3K in the endogenous mass spectrometric analysis is due to the RAS10 antibody binding the Switch I domain, preventing effector binding (Figure S1C). The lack of other RAS regulators like SOS1 and NF1 that associate with RAS through the Switch II domain may be due to their transient association and plasma-membrane-localized/cell-specific expression. Interestingly, we did not detect peptides spanning AGO2 in our earlier mass-spectrometric-based studies involving ERG, PRC complex protein EED (Brenner et al., 2011; Cao et al., 2014), and at least four other protein pull-down data sets (data not shown), indicating the specificity of AGO2 coIP with RAS. Analyzing the RAS coIP MS data further, we noted peptides mapping uniquely to all three RAS family members, namely KRAS, NRAS, and HRAS, were readily detected across the cell line panel (Figure 1B). In contrast, almost all uniquely mapping peptides to AGO family proteins were specific to AGO2 in all of the 12 cell lines (except for a single unique peptide that mapped to AGO1 in one sample; Figure 1B).

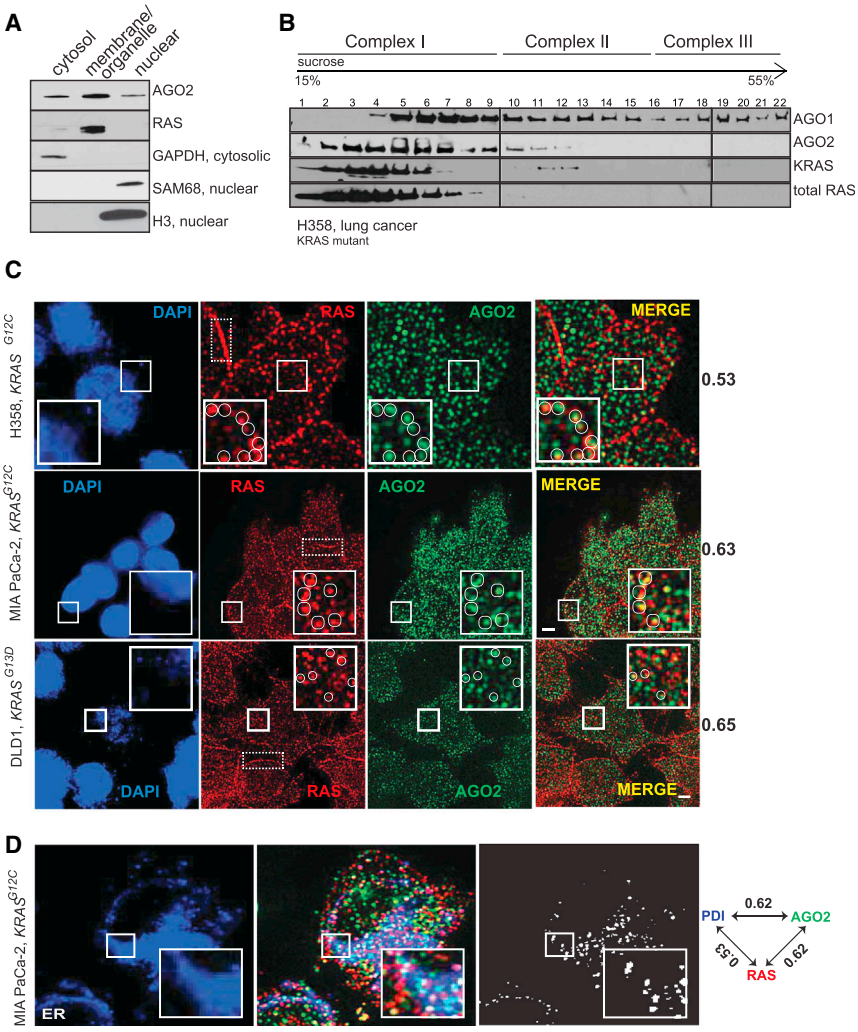

Figure 2. Co-sedimentation and Co-localization of RAS and AGO2 in the Endoplasmic Reticulum

(A) Cell fractionation analysis of H358 cells to show enrichment of distinct proteins in the cytosolic/membrane or organelle/nuclear fractions. GAPDH was used as a cytosolic marker whereas SAM68 and H3 histone were used as nuclear markers.

(B) Sucrose density gradient fractionation of cell lysates from H358 cells followed by immunoblot detection of total RAS, KRAS, AGO1, and AGO2 proteins.

(C) Representative images of immunofluorescence analysis of RAS (red) and AGO2 (green) in H358, MIA PaCa-2, and DLD-1 cells. Yellow spots in merged images indicate perinuclear co-localization of RAS and AGO2. The nucleus was visualized by DAPI staining (blue). Dotted boxes highlight plasma membrane regions predominantly localized by RAS. Manders overlap coefficient in the intracellular regions of the cells is indicated on the right. An overlap coefficient of 0 suggests no co-localization, whereas a value of 1 indicates complete co-localization. The inset shows a magnified 5.3 × 5.3 μm view of the areas marked. Images are pseudocolored maximum intensity projections (across 2.5 μm), obtained from 3D imaging. The scale bar represents 5 μm.

(D) Representative images of immunofluorescence analysis of AGO2 (green), RAS (red), and ER marker, PDI, (blue) in MiaPaCa-2 cells. White spots indicate co-localization signals for RAS/AGO2/PDI in each panel. Pairwise Manders overlap coefficients are shown on the right. The inset shows a magnified 6.7 × 6.7 μm view of the areas marked. The scale bar represents 5 μm.

See also Figure S2.

The putative endogenous interaction between RAS and AGO2 was corroborated by reciprocal IPs using two different antibodies for each, in two different lung cancer cell lines, H358 and H460, harboring distinct *KRAS* mutations (Figure 1C). Further, consistent with the coIP MS analyses (Figure 1A), the RAS-AGO2 interaction was readily detected by coIP followed by immunoblot analysis in two cell lines with wild-type *KRAS* and representative lung and pancreatic cancer cells harboring various activating mutations of *KRAS* (Figure 1D). The observed RAS-AGO2 interaction was maintained even under highly stringent conditions of 1 M NaCl (Figure S1E). The RAS-AGO2 coIP was maintained in the presence of RNase, suggesting that the interaction is independent of AGO2 interaction with RNA (Figures S1F and S1G). To demonstrate further specificity of this interaction, we overexpressed FLAG-tagged *AGO2* construct in HEK293 cells and detected RAS in FLAG immunoprecipitates (Figure S1H). We also performed the coIP analysis in genetically engineered "*RAS*less" mouse embryonic fibroblast cells (Drosten et al., 2010) and failed to detect this interaction upon ablation of KRAS expression (Figure S1I), further establishing the specificity of the RAS-AGO2 interaction.

Co-localization of RAS and AGO2 in the Membrane Component of Endoplasmic Reticulum

RAS proteins are known to localize to the plasma membrane and membranes of various intracellular organelles like the endoplasmic reticulum (ER), Golgi, and mitochondria with distinct signaling outputs (Bivona et al., 2006; Prior and Hancock, 2012). AGO2 is known to assemble in the ER (Kim et al., 2014; Stalder et al., 2013), cytoplasm (Höck et al., 2007), and nucleus (Dudley and Goldstein, 2003; Gagnon et al., 2014). Consistent with this observation, fractionation of H358 cells revealed that RAS was restricted mainly to the membrane (plasma membrane and endomembrane) fraction along with AGO2, which was also detected in the cytoplasmic and nuclear extracts (Figure 2A). Sedimentation analyses using sucrose density gradient showed that total RAS and mutant KRAS predominantly co-sedimented with AGO2 in smaller-molecular-weight fractions (Complex I; Figure 2B) as defined by a previous study (Höck et al., 2007).

Next, to assess co-localization of endogenous RAS and AGO2, we performed indirect immunofluorescence using RAS10 and AGO211A9 (Rüdel et al., 2008) antibodies in

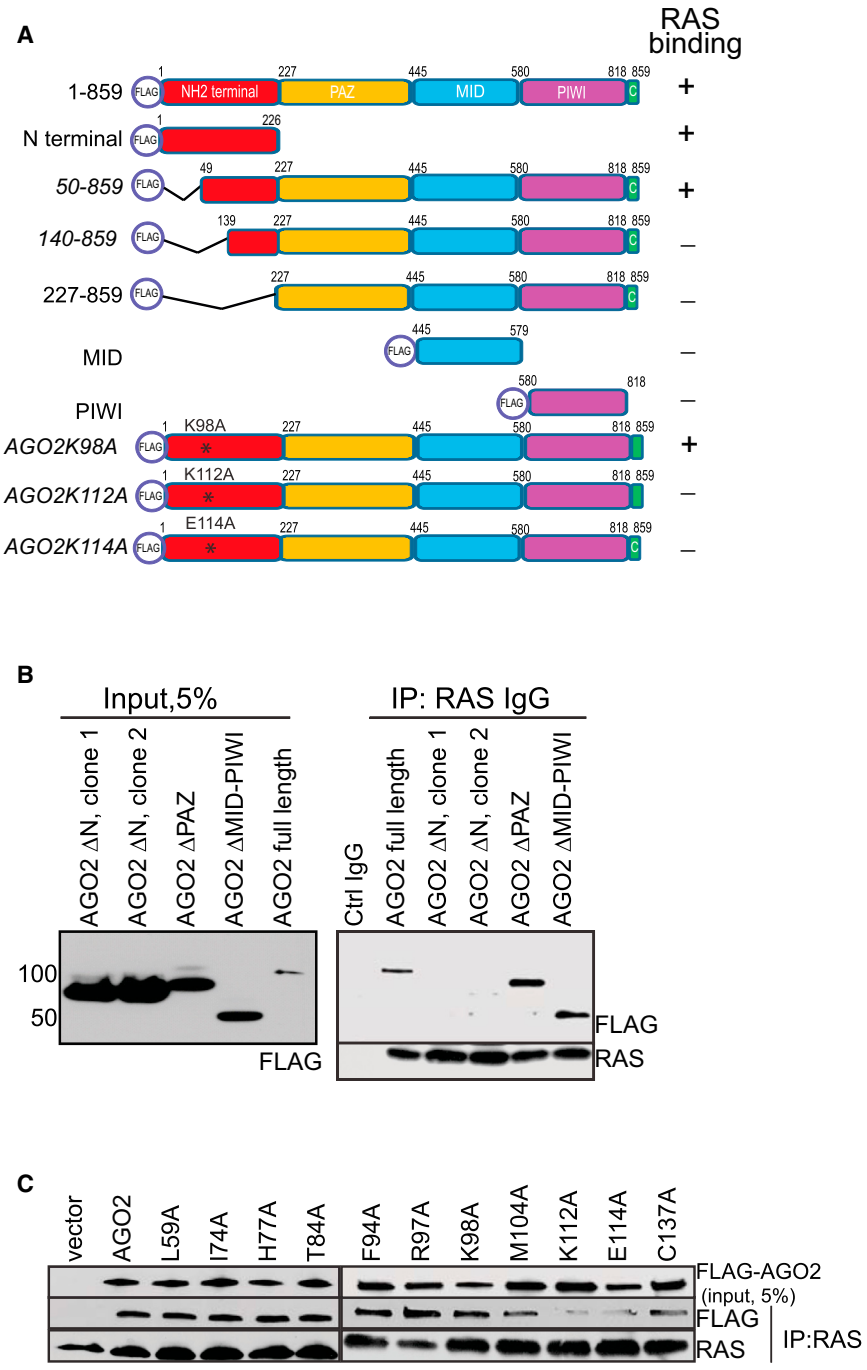

Figure 3. The N-Terminal Domain of AGO2 Interacts with RAS

(A) Schematic summary of FLAG-tagged *AGO2* deletion and mutant constructs used for RAS coIP analyses.

(B) Expression of FLAG-tagged N-terminal, PAZ, or PIWI domains of *AGO2* in HEK293 cells (left), followed by RAS IP (right). Immunoblot analysis shows that deletion of (1–226 aa) N-terminal domain in AGO2 abrogates RAS interaction.

(C) Expression of indicated *AGO2* N-terminal point mutant constructs within the wedge domain (50–139 aa) in HEK293 cells, followed by RAS coIP analysis.

See also Figure S3.

different cells. To ascertain the specificity of RAS10 Ab, antigenic peptides were used for competition prior to immunofluorescence analysis (Figure S2A); in addition, AGO211A9 has been demonstrated to be a highly specific, validated monoclonal antibody for immunofluorescence detection of AGO2 (Rüdel et al., 2008). In H358, MIA PaCa-2, and DLD-1 cells (Figure 2C), RAS staining was visible both at the plasma membrane and intracellular regions, whereas only cytoplasmic staining was detected for AGO2. Manders co-efficient analysis indicative of signal overlap between the two proteins was determined to be 0.53, 0.65, and 0.60 in H358, MIA PaCa-2, and DLD-1 cells, respectively (where 1 is considered complete overlap and 0 is considered no overlap). These findings suggest significant co-localization of RAS and AGO2 predominantly in the intracellular perinuclear regions of cells (Figure 2C).

Given that cytoplasmic RAS is restricted to the endomembrane bound organelles, we performed a three-color immunofluorescence staining for RAS and AGO2 along with specific protein markers of different organelles in MIA PaCa-2 cells. Whereas we observed a significant signal overlap between RAS, AGO2, and ER marker (PDI; Figures 2D and S2B), Manders coefficient values were minimal for Golgi (RCAS1), endosomal (Rab5/7/11), or mitochondrial (COX4) markers (Figures S2B and S2C). This suggests that endogenous RAS and AGO2 are predominantly found in the ER (Manders coefficient for both RAS in ER and AGO2 in ER was 0.62 each), where they co-localize. Hence, along with the cell fractionation analyses, these immunofluorescence data suggest that a subset of RAS proteins co-localizes with AGO2 in the endomembranous components of the ER.

AGO2 Binds RAS through Its N-Terminal Wedge Domain

To identify specific region(s) in AGO2 involved in the interaction with RAS, we employed a panel of FLAG-epitope-tagged AGO2 expression constructs (summarized in the schematic in Figure 3A). RAS coIP analysis of the FLAG-tagged AGO2 deletion constructs showed that the N-terminal domain of AGO2

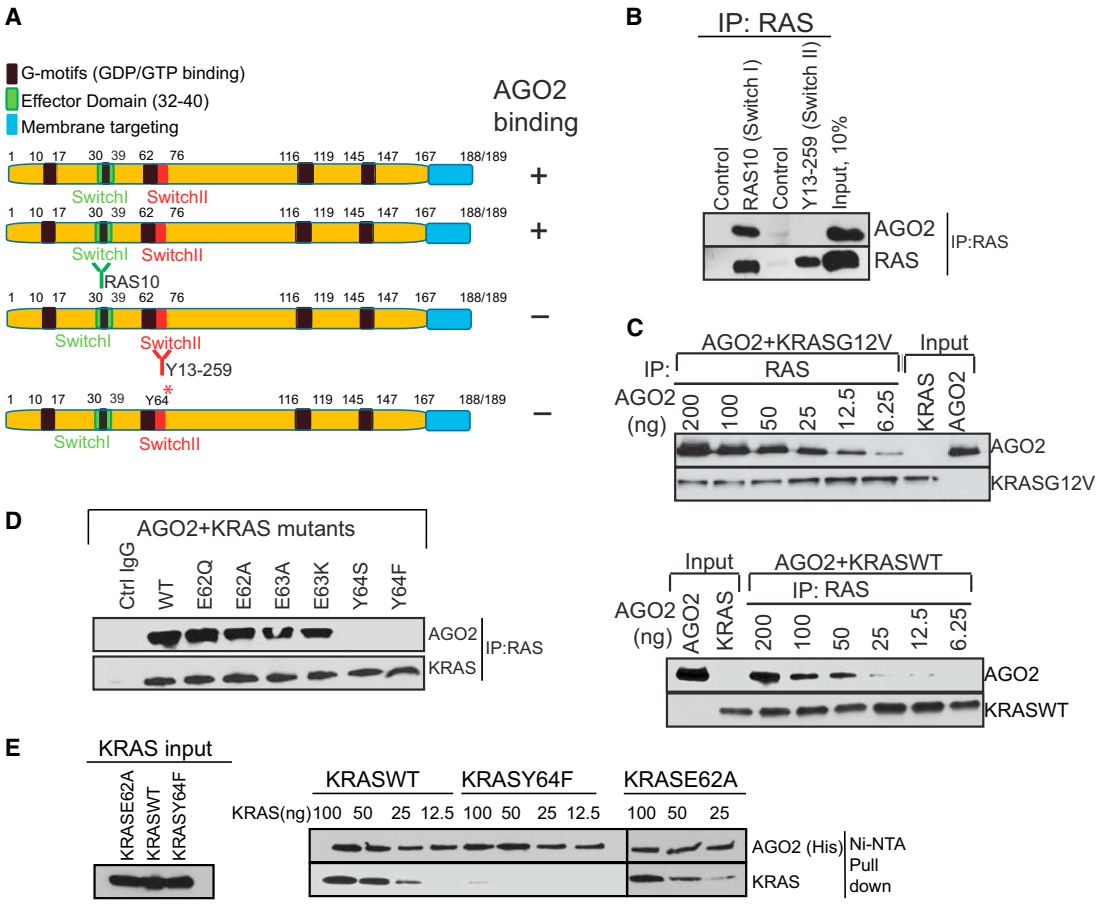

Figure 4. The Switch II Domain of RAS Interacts with AGO2

(A) Schematic summary of the antibodies and recombinant proteins used for RAS-AGO2 coIP analysis to identify residues in RAS, critical for AGO2 interaction. (B) RAS coIP using antibodies that bind Switch I domain (RAS10 Ab) or Switch II domain (Y13-259 Ab), followed by immunoblot analysis for RAS and AGO2. (C–E) Characterization of direct RAS-AGO2 interaction, in vitro. (C) Immunoblot analysis following in vitro coIP of recombinant KRASG12V (top) and KRASWT (bottom) in the presence of varying concentrations of recombinant AGO2 is shown. (D) In vitro coIP analysis of KRAS-AGO2 interaction using a panel of KRAS mutant proteins spanning amino acid residues 62–65 in the Switch II domain is shown. (E) Immunoblot analysis following His-AGO2 pull-down assay using Ni-NTA beads upon incubation with different KRAS mutant proteins is shown.

See also Figure S4.

was necessary (Figure 3B) and sufficient (Figure S3A) for RAS binding. Further analysis of a panel of deletion constructs spanning the N-terminal domain suggested that the region spanning 50–139 aa was critical for RAS binding (Figure S3B). Interestingly, this aa stretch was recently shown to be part of the "wedging" domain, important for microRNA duplex unwinding prior to RISC assembly (Kwak and Tomari, 2012). To further define AGO2 residues critical for interaction with RAS, we focused on the 50–139 aa stretch that is uniquely present in AGO2 (and not in AGO1, 3, or 4) based on the fact that, among the Argonaute family proteins, AGO2 was almost singularly represented in the RAS coIP MS data. ClustalW alignment of all human Argonaute proteins (AGO1–4) identified ten residues unique to AGO2 in this region (Figure S3C). Alanine substitution of each of the ten residues was followed by RAS coIP analysis, and aa K112 and E114 of AGO2 were found to be critical for a direct association with RAS (Figure 3C).

Y64 Residue within the Switch II Domain of KRAS Is Critical for Direct AGO2 Binding

In a parallel analysis aiming to define the residues in RAS critical for AGO2 association, we first employed two RAS antibodies that bind exclusively either to the Switch I (RAS10 mAb) or the Switch II (Y13-259) domains (summarized in Figure 4A). Whereas both antibodies efficiently immunoprecipitated RAS in H358 cell lysates, AGO2 was present only in IPs with Switch-I-specific RAS10 Ab and not in Switch-II-specific Y13-259 Ab (Figure 4B), suggesting that the Switch II domain in RAS is critical for AGO2 interaction. Next, we hypothesized that, if the RAS-AGO2 interaction is restricted through contacts with the Switch II domain, we may be able to detect AGO2 in RAS-GTP complexed with RAF, on RAS-binding domain (RBD) agarose beads. As predicted, we were able to detect AGO2 on RAS-GTP bound to RBD-agarose in H358 ($KRAS^{G12C}$) cells (Figure S4A), further supporting that AGO2 binds to the Switch II domain of GTP-bound KRAS.

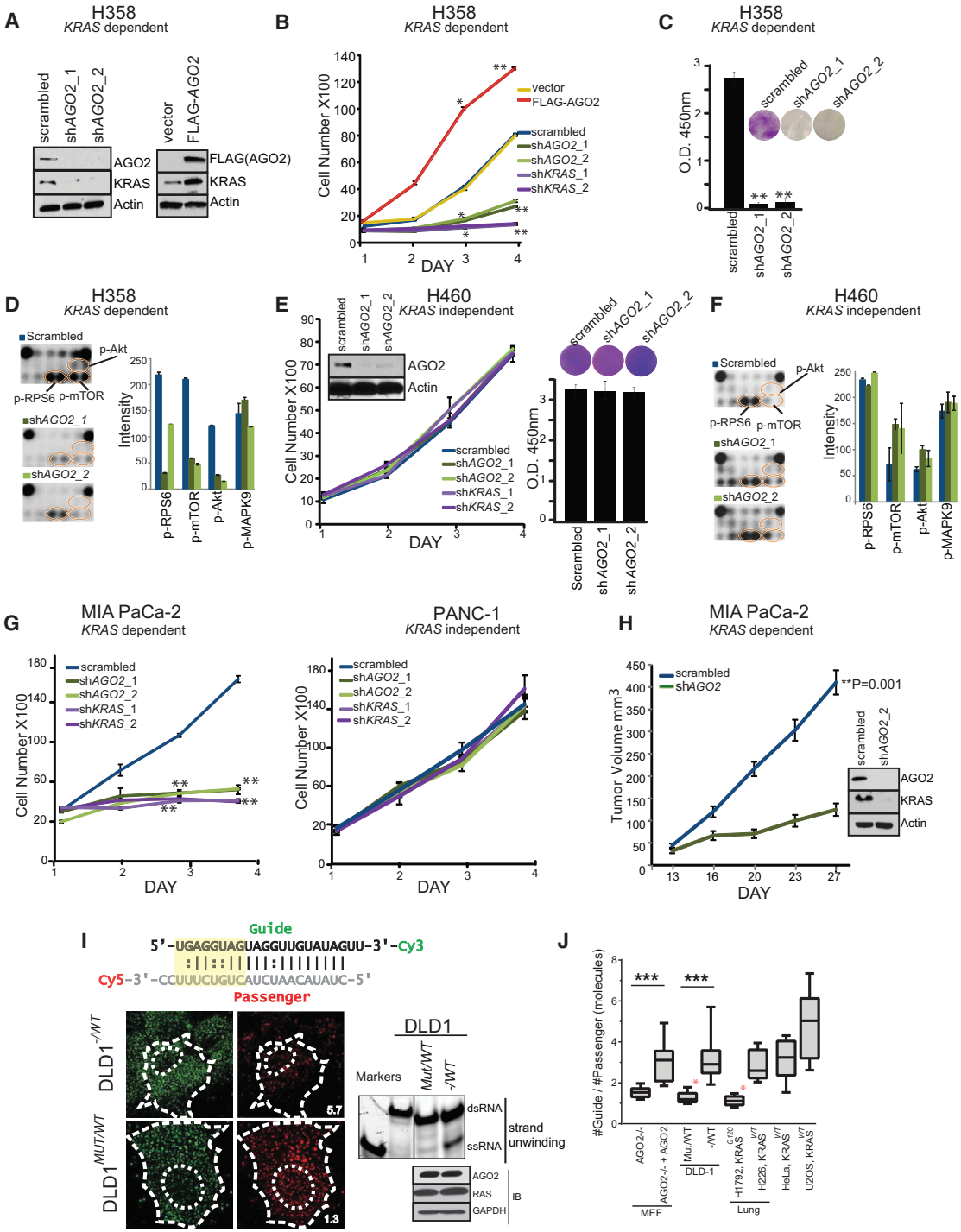

Figure 5. *AGO2* Is Essential for Mutant *KRAS*-Dependent Cell Proliferation

(A) Immunoblot analysis of AGO2 and KRAS after knockdown or overexpression of *AGO2*.

(B and C) Growth curves (B) and colony formation assays (C) of mutant *KRAS*-dependent H358 lung cancer cells, following either knockdown of *KRAS*/*AGO2* using shRNA or *AGO2* overexpression. Error bars are based on SEM. *($p < 0.05$) and **($p < 0.005$) denote significant differences in growth at the indicated times compared to either scrambled or vector control. Data were obtained from three independent experiments.

(D) Pathscan intracellular signaling arrays probed with lysates from H358 cells following *AGO2* knockdown.

(E) Growth curves (left) and colony formation assays (right) of mutant *KRAS*-independent H460 lung cancer cells, following knockdown of *KRAS*/*AGO2*. Data obtained from three independent experiments are shown. Inset shows immunoblot analysis of AGO2 and KRAS upon *AGO2* knockdown.

(F) Intracellular signaling array probed with lysates from H460 following *AGO2* knockdown.

(legend continued on next page)

Next, we sought to determine the specific residues in the Switch II region of KRAS involved in its interaction with AGO2, using in vitro coIP assays. Purified recombinant KRASG12V or KRASWT proteins were incubated with varying concentrations of AGO2 protein followed by RAS immunoprecipitation. We observed a concentration-dependent, direct interaction between recombinant AGO2 and both the wild-type and mutant KRAS proteins (Figure 4C). Further, in vitro coIP of recombinant AGO2 protein with the panel of Switch II mutant KRAS proteins showed that altering the Y64 residue (but not the neighboring aa) significantly reduced KRAS binding to AGO2 (Figure 4D). To further substantiate this observation, and to obviate potential technical concerns inherent in antibody-based coIP, we carried out an antibody-independent pull-down assay using recombinant His-tagged AGO2 protein bound to Ni-NTA beads. Consistent with the in vitro coIP analyses, the His-tagged AGO2 pull-down assay also showed specific dependency of AGO2-RAS binding on the Y64 residue (Figure 4E).

To assess whether GDP/GTP loading of KRAS may influence the AGO2 interaction in vitro, we carried out in vitro coIP analyses using KRASWT and KRASG12V proteins loaded with GDP/GTPγS and as seen in Figure S4B. Our results showed that AGO2 binding was agnostic to nucleotide loading status of KRAS. Similarly, both the KRASWT and KRASG12V proteins were observed to bind to His-tagged AGO2, independent of the nucleotide loading on KRAS (Figure S4C). To validate the efficiency and specificity of nucleotide loading onto KRAS proteins, we performed RAF-RBD pull-down assays and observed the expected differential between GDP- and GTP-bound KRAS with respect to RAF-RBD binding (Figure S4D). Thus, these data define the aa in RAS (Y64) and AGO2 (K112/E114) as critical for the RAS-AGO2 interaction.

Reduced RISC Activity Elevates Oncogenic KRAS Levels, Making AGO2 Essential for Mutant KRAS-Dependent Cell Proliferation

Next, we set out to analyze functional implications of the RAS-AGO2 interaction, particularly in the context of KRAS-driven transformation. To this end, we first carried out knockdown of *AGO2* in H358 lung cancer cells that harbor a homozygous *KRAS* mutation and are known to be *KRAS* dependent (Symonds et al., 2011). Whereas the microRNA *let-7*/AGO2 axis is reported to negatively regulate wild-type RAS levels (Diederichs and Haber, 2007; Johnson et al., 2005), we observed a remarkable reduction in mutant KRAS protein levels in H358 cells with *AGO2* knockdown (Figure 5A, left panel). Conversely, overexpression of *AGO2* in the same cells led to elevated levels of KRAS, implying a positive regulation of mutant KRAS levels by AGO2 (Figure 5A, right panel). Consistent with these observations, knockdowns of *AGO2* and/or *KRAS* in H358 cells (using two independent shRNAs; Figures S5A and S5B) showed reduced rates of cell proliferation whereas AGO2 overexpression resulted in increased cell proliferation (Figure 5B). Furthermore, *AGO2* knockdown reduced the ability of H358 cells to form colonies in colony formation assays (Figure 5C) and resulted in a marked reduction in levels of known mediators of KRAS signaling, including p-Akt, p-mTOR, and p-RPS6 based on our analysis with Pathscan intracellular signaling array (Cell Signaling Technology; Figures 5D, S5C, and S5D). Interestingly, similar *AGO2* depletion experiments (using the same shRNAs described above) in *KRAS*-independent H460 lung cancer cells, which also harbors a mutant *KRAS*, did not affect cell proliferation, colony formation (Figure 5E), or intracellular signaling (Figures 5F and S5E). Phenotypic effects upon *AGO2* knockdown in the context of *KRAS* dependency were also observed in pancreatic cancer cell lines, where knockdown of either *KRAS* or *AGO2* dramatically reduced cell proliferation in mutant *KRAS*-dependent MIA PaCa-2 cells, but not in mutant *KRAS*-independent PANC-1 cells (Figures 5G, S5A, and S5B). Further, *AGO2*-depleted MIA PaCa-2 cells failed to establish xenografts in SCID mice (Figure 5H), with a concomitant reduction in KRAS protein levels (Figure 5H, inset). These data suggest that *KRAS*-dependent cancer cells manifest a coincident dependence on *AGO2* to maintain oncogenic KRAS protein levels and support a functional role for *AGO2* in potentiating the oncogenic activities of mutant *KRAS*.

To directly address the consequence of mutant KRAS binding at the N-terminal of AGO2, critical for microRNA duplex unwinding (Kwak and Tomari, 2012; Wang et al., 2009), we performed *let-7* unwinding assays in isogenic colorectal cancer cells, DLD-1, harboring heterozygous $KRAS^{G13D}$ (MUT/WT) alleles or wild-type KRAS (−/WT). Dually labeled double-stranded *let-7a* (Figure 5I, schematic) was injected and assessed for the extent of single strand formation. Quantitation of the

(G) Growth curves of pancreatic cancer cells, MIA PaCa-2 (mutant KRAS dependent; left), and PANC-1 (mutant KRAS independent; right) following knockdown of *KRAS* or *AGO2*, as indicated. *($p < 0.05$) and **($p < 0.005$) denote significant differences in growth at the indicated times compared to scrambled control. Data were obtained from three independent experiments.

(H) In vivo growth of Mia PaCa-2 cells transiently treated with either scrambled shRNA or shRNA targeting *AGO2* prior to injecting in nude mice. For each group ($n = 8$), one million cells were injected and average tumor volume (in mm^3) was plotted on y axis and days after injection on the x axis. Right shows immunoblot analysis of AGO2 and RAS following *AGO2* knockdown in Mia PaCa-2 cells. Indicated p value was calculated using two-sided Student's t test for the two groups.

(I) (Top) Schematic of the labeled *let-7* microRNA used in the intracellular strand unwinding assays. Straight lines and double dots represent Watson-Crick and Wobble pairs, respectively. The thermodynamically unstable end (highlighted in yellow) promotes asymmetric loading of the guide strand. (Bottom left) Representative images of the guide strand (green) and passenger strand (red) of *let-7* microRNA, 30 min post-intracellular injections in DLD-1 isogenic lines, expressing wild-type KRAS (−/WT) or $KRAS^{G12C}$ (MUT/WT) are shown. Numbers represent the guide:passenger strand ratio. Ratio of 1:1 indicates attenuation of *let-7* dsRNA unwinding whereas a higher guide:passenger strand ratio indicates efficient unwinding and functional RISC. The scale bar represents 10 μm. (Bottom right) Native acrylamide gel electrophoresis of *let-7* unwinding assay and immunoblot analysis of DLD-1 isogenic cell line extracts is shown. M1 and M2 represent double- (ds) and single-stranded (ss) markers, respectively.

(J) Box plot representing the guide:passenger strand ratio in the indicated cell lines with varying *KRAS* mutation status. Whiskers represent minimum and maximum values, and line represents median of the data set ($n \geq 2$; no. cells ≥ 13; ***$p < 0.0005$). Red asterisk indicates cells expressing mutant KRAS.

See also Figure S5.

guide-to-passenger strand ratio was estimated 30 min after injection, where a 1:1 ratio was considered as no unwinding whereas higher ratios indicate active unwinding. As seen in Figure 5I (left), the formation of single-stranded (ss) RNA molecules from double-stranded (ds) *let-7* substrates, a key step in the formation of active RISC, was attenuated in DLD-1 MUT/WT cells (ratio = 1.3). Duplex unwinding was restored in isogenic cells lacking mutant KRAS (−/WT; ratio = 5.7). Biochemical assays using cellular lysates followed by gel electrophoresis also showed reduced *let-7* unwinding in DLD-1 MUT/WT cells (Figure 5I, right), even though the RAS-AGO2 interaction was detected in both DLD-1 isogenic cells (Figure S5F). Additionally, the *let-7* unwinding assay was performed in mouse embryonic fibroblasts lacking AGO2 (MEF*AGO2*−/−) and *MEFAGO2*−/− reconstituted with AGO2 (MEF*AGO2*−/− + *AGO2*; Broderick et al., 2011) to demonstrate that the microRNA unwinding assay is AGO2 dependent (Figures S5G and S5H). Further, to circumvent any artificial effects of gene knockout models, we subjected multiple cancer cells, naturally harboring different KRAS alleles, to the same *let-7* unwinding assay. As seen in Figures 5J and S5I, only oncogenic KRAS-expressing cells showed reduced *let-7* unwinding, indicative of diminished AGO2 function in cells harboring mutations in *KRAS*.

Mutant KRAS-AGO2 Interaction Promotes Cellular Transformation

To address the mechanistic underpinnings of the phenotypic effects associated with the mutant KRAS-AGO2 interaction, we employed the classic NIH 3T3 experimental model system to ectopically express human $KRAS^{WT}$ or $KRAS^{G12V}$ (Qiu et al., 1995; Shih et al., 1981), with or without *AGO2*, and carried out transient foci formation assays. As expected, no foci were observed in cells transfected with $KRAS^{WT}$, as well as in cells with $KRAS^{WT}$ ± *AGO2*. However, NIH 3T3 cells transfected with $KRAS^{G12V}$ generated characteristic foci of transformed cells. Remarkably, co-transfection of $KRAS^{G12V}$ with AGO2 enhanced the number of foci by approximately 5-fold, compared to the vector control (Figure 6A). In contrast, *AGO2* overexpression did not enhance $BRAF^{V600E}$-driven focus formation (Figure S6A), suggesting that *AGO2* specifically potentiates RAS-mediated oncogenesis, most likely as a result of its direct interaction with RAS. In vivo experiments using a mouse xenograft model also showed a significant increase in tumor growth with cells expressing $KRAS^{G12V}$+*AGO2* compared to $KRAS^{G12V}$+vector control (Figure S6B). As expected, in these experiments, cells expressing either $KRAS^{WT}$ or *AGO2* alone did not develop tumors. Consistent with *AGO2* overexpression in H358 cells (Figure 5A), immunoblot analysis of NIH 3T3 cells overexpressing *AGO2* showed an increase in KRAS protein levels (Figure 6B).

To understand the effects of AGO2 on the RAS-signaling pathways, we analyzed protein lysates from NIH 3T3 cells stably expressing $KRAS^{G12V}$+vector or $KRAS^{G12V}$+*AGO2* using the Pathscan intracellular signaling arrays. Cells expressing $KRAS^{G12V}$+*AGO2* showed a marked increase in the levels of p-Akt, p-mTOR, p-RPS6, and p-BAD, but not phospho-ERK (Figures 6C, right panel, S5C, and S5D), suggesting that the increased levels of oncogenic KRASG12V protein signals largely through PI3K activation.

Exploiting the NIH 3T3 overexpression model to probe the reciprocal effects of mutant KRAS on AGO2 function, we profiled microRNAs from foci obtained from $KRAS^{G12V}$+vector and $KRAS^{G12V}$+*AGO2* using high-throughput sequencing. Whereas AGO2 overexpression is known to elevate levels of mature microRNAs (Diederichs and Haber, 2007), we observed a marked reduction in microRNA levels (214/781) in $KRAS^{G12V}$+*AGO2*-expressing foci, including most of the *let-7* family members (Figure S6E). Interestingly, a small proportion (27/781) of microRNAs was elevated and included known "oncomiRs" *miR-221* and *miR-222*. microRNA qPCR analysis of NIH 3T3 cells expressing *AGO2* alone or $KRAS^{WT}$/$KRAS^{G12V}$ ± *AGO2* also showed reduced *let-7* levels only in the $KRAS^{G12V}$ +*AGO2*-expressing cells (Figure S6F), suggesting an inhibition of AGO2 function in oncogenic KRAS-expressing cells.

To further investigate a requirement for an AGO2 interaction in $KRAS^{G12V}$-driven transformation, we first performed in vitro RAS coIP assays using mutant KRASG12D and the double mutant KRASG12DY64G, which has previously been shown to have limited oncogenic potential (Shieh et al., 2013). Whereas KRASG12D binds AGO2, KRASG12DY64G failed to bind AGO2 (Figure S6G). Transfecting a retroviral vector encoding $KRAS^{G12VY64G}$ double mutant into NIH 3T3 cells failed to generate foci (Figure 6D). As an important corollary to our hypothesis that mutant KRAS-AGO2 interaction leads to elevated mutant KRAS protein levels, the $KRAS^{G12VY64G}$ stably expressing cells also showed much-lower levels of KRAS protein than $KRAS^{G12V}$-expressing cells (Figure 6E, top panel). An independent construct encoding $KRAS^{G12VY64G}$ showed similar results despite high levels of KRAS transcript expression (Figures S6H–S6J). Curiously, RBD assays suggest that expressed $KRAS^{G12VY64G}$ was GTP loaded and activated phospho-Akt and phospho-ERK similar to $KRAS^{G12V}$, suggesting that, although $KRAS^{G12VY64G}$ levels are low, it is GTP loaded and likely signaling at the membrane. Yet, despite expressing activated RAS, NIH 3T3 stable cells expressing $KRAS^{G12VY64G}$ failed to show the characteristic morphology of $KRAS^{G12V}$ cells (Figure 6E, bottom panel). In vivo, these cells also failed to establish tumors in the xenograft mouse model (Figure 6F), supporting a critical role for Switch II region (Y64) in KRAS-driven transformation, including its association with AGO2.

Whereas NIH 3T3 cells stably expressing $KRAS^{G12V}$ showed reduced *let-7* levels, $KRAS^{G12VY64G}$-expressing cells, which do not allow for the mutant KRAS-AGO2 interaction, showed no change in *let-7* expression, providing evidence for a direct role of mutant KRAS in the modulation of microRNA levels in this model (Figure S6K). Cognate analysis of the levels of *let-7* target transcripts (Lee and Dutta, 2007) showed an almost log-fold change in the mRNA levels of *HMGA1* and *HMGA2* only in $KRAS^{G12V}$-expressing cells (Figure S6L). Together, our data using the $KRAS^{G12VY64G}$ mutant and *let-7* levels as readout of AGO2 function broadly support the conclusion that mutant KRAS, through its direct association, inhibits AGO2 activity.

To more directly explore the potential effect of $KRAS^{G12V}$ on functional messenger ribonucleoprotein particles (mRNPs), we exploited a recently described method for intracellular single-molecule, high-resolution localization and counting (iSHiRLoC)

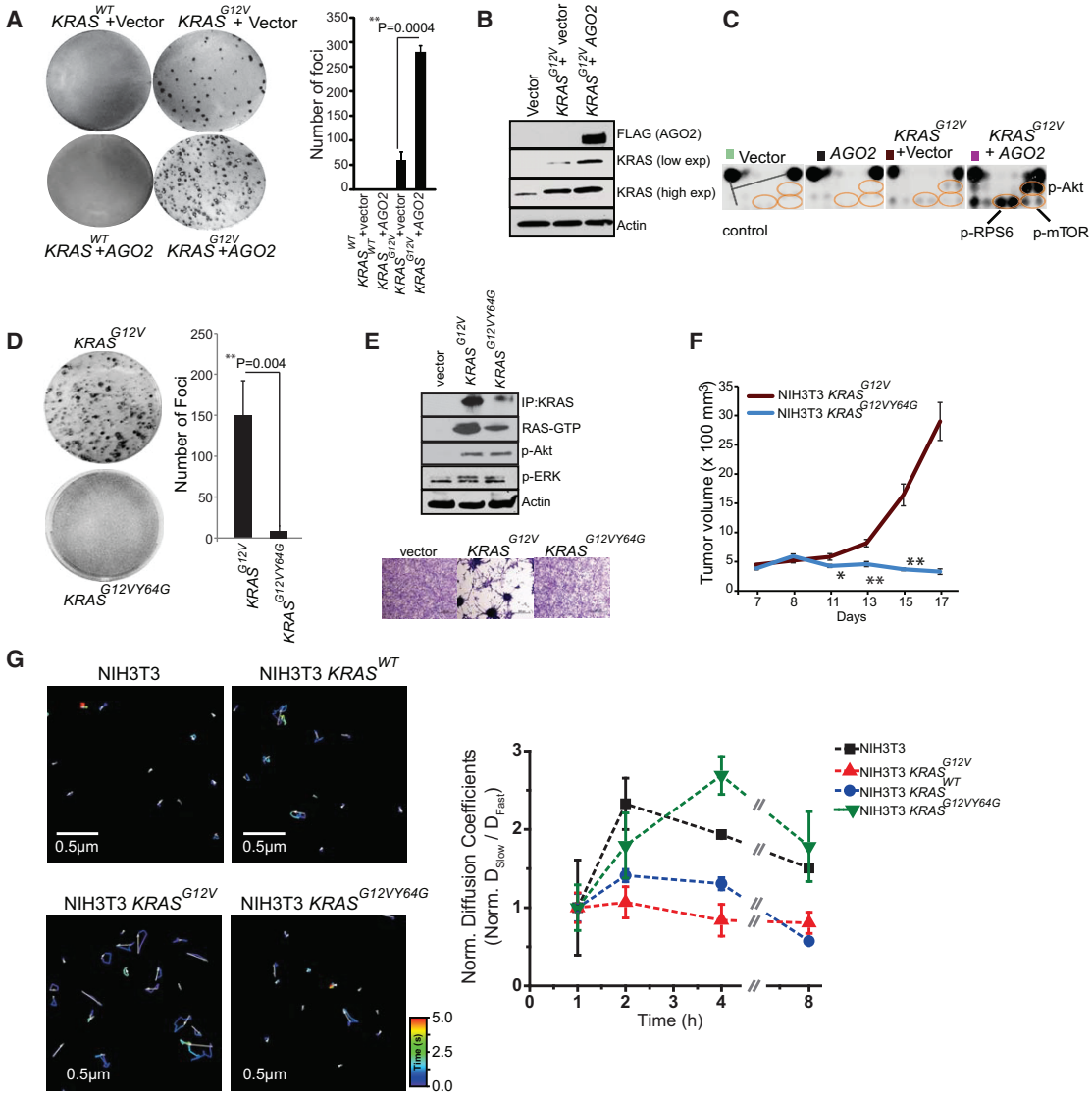

Figure 6. Mutant KRAS-AGO2 Interaction Promotes Transformation

(A) Representative images of foci formation assays using NIH 3T3 cells co-transfected with KRAS^{WT} or *KRAS*^{G12V} and *AGO2* (left panel). Quantitation of foci from two technical replicate experiments (right panel) is shown. Foci assays were performed at least three times with similar results. p value was calculated using two-sided Student's t test between the two groups.

(B) Immunoblot analysis shows increased levels of oncogenic KRAS levels in the presence of AGO2.

(C) Intracellular signaling arrays probed with lysates from NIH 3T3 cells stably expressing vector, *AGO2*, or *KRAS*^{G12V} ± *AGO2*. The colored circles mark duplicate spots corresponding to p-AKT (S473), p-RPS6 (S235/236), and p-mTOR (S2448).

(D) Representative images of foci formation assays using NIH 3T3 cells co-transfected with *KRAS*^{G12V} or *KRAS*^{G12VY64G}. Quantitation of foci from two independent experiments (right) is shown. Indicated p value was calculated using two-sided Student's t test.

(E) KRAS immunoprecipitation (using sc-521 pAb) followed by immunoblot analysis (RAS10 Ab) showing low levels of oncogenic KRAS protein expression in NIH 3T3 cells stably expressing *KRAS*^{G12VY64G}. RAS-GTP levels were assessed using RBD agarose beads. Signaling through phospho-Akt and phospho-ERK activation was performed after serum starvation by immunoblot analysis. Lower panel shows morphology of indicated stable lines grown in 10% serum upon crystal violet staining.

(F) In vivo growth of NIH 3T3 cells stably overexpressing *KRAS*^{G12V} and *KRAS*^{G12VY64G} in nude mice. For each group (n = 8), 500,000 cells were injected and average tumor volume (in mm^3) was plotted on y axis and days after injection on the x axis.

(G) (Left) Representative 3.14 × 3.14 µm^2 regions from NIH 3T3 (top left), NIH 3T3-*KRAS*^{WT} (top right), NIH 3T3-*KRAS*^{G12V} (bottom left), and NIH 3T3-*KRAS*^{G12V,Y64G} cells (bottom right) that were imaged 4 hr (h) after microinjection of let-7-a1-Cy5. Individual particle tracks (colored) and their net displacements (white arrow) over a 5-s period (time; color bar) are shown. Shorter displacement vectors indicate let-7 assembly in larger mRNP complexes with less mobility, whereas longer white arrows indicate let-7 assembly in smaller mRNP complexes with high mobility. (Right) Graphical representation of ratio of "slow"-moving complexes (particles with diffusion coefficients <0.06 µm^2/s) and "fast"-moving complexes (particles with diffusion coefficients >0.06 µm^2/s), normalized to the first hour time point, are plotted as a function of time.

See also Figure S6.

of microRNAs (Pitchiaya et al., 2012, 2013). Diffusion coefficients of microinjected fluorophore-labeled *let-7a* molecules suggest that, in NIH 3T3 cells expressing $KRAS^{WT}$, *let-7a* assembles into both "fast" (low molecular weight) and "slow" (high molecular weight) mRNA-protein complexes (mRNPs; Figures 6G and S6M). By contrast, in cells expressing $KRAS^{G12V}$, *let-7a* manifested predominantly in fast-moving complexes, suggesting that *let-7a* is unable to accumulate in larger mRNPs (known to be functional RISC; Pitchiaya et al., 2012, 2013) in an oncogenic *KRAS* setting. Importantly, in cells expressing $KRAS^{G12VY64G}$, *let-7a* accumulates in both fast and slow mRNPs, further implicating that a direct interaction between mutant KRAS and AGO2 is essential to prevent functional RISC assembly. Thus, the NIH 3T3 overexpression model suggests that, through its interaction with AGO2, mutant KRAS modulates levels of mature microRNAs likely due to its ability to inhibit an early step of RISC assembly.

AGO2 Interaction Is Required to Maximize Oncogenic Potential of Mutant KRAS

To further underscore the role of AGO2 in $KRAS^{G12V}$-driven oncogenesis, we generated NIH 3T3 cells with *AGO2* knockout (NIH 3T3 *AGO2*−/−) using the CRISPR/Cas9 methodology (Ran et al., 2013; Figure S7A). Validation of *AGO2* knockout in NIH 3T3 *AGO2*−/− cells was performed at the DNA, RNA, and protein levels (Figures S7B–S7D). Sucrose density sedimentation analysis of NIH 3T3 *AGO2*−/− showed that, in contrast to NIH 3T3 parental cells, RAS is restricted largely to the first four fractions of the gradient with minimal overlap with AGO1 complexes, indicating that RAS associates with higher-molecular-weight fractions through its interaction with AGO2 (Figure 7A). NIH 3T3 *AGO2*−/− cells had lower levels of *let-7* family microRNAs (Figure S7E), consistent with previous studies demonstrating that a loss of AGO2 results in reduction of absolute levels of all microRNAs (Diederichs and Haber, 2007). In NIH 3T3 *AGO2*−/− cells, the reduction of *let-7* family microRNA levels also resulted in a concomitant increase in *let-7* target (*HMGA1*/*HMGA2*) transcript levels (Figure S7F).

Despite reduced levels of microRNAs, $KRAS^{G12V}$ expression in the NIH 3T3 *AGO2*−/− cells showed a markedly reduced ability to generate foci compared to parental NIH 3T3 (Figures 7B and S7G). Partial rescue of the ability to establish foci in these cells was achieved by overexpression of *AGO2* or $AGO2^{K98A}$ (which permits RAS interaction), but not the $AGO2^{K112A}$ mutant (which does not bind RAS; Figure 3C). These observations also support the notion that a direct association of oncogenic KRAS and AGO2 is required for mutant KRAS-driven transformation. In addition, NIH 3T3 *AGO2*−/− cells stably expressing $KRAS^{G12V}$ did not display the characteristic morphology of NIH 3T3 $KRAS^{G12V}$ cells (Figure 7C, top panel). In vivo experiments in a mouse xenograft model also showed significantly decreased tumor growth, with NIH 3T3 AGO2−/− cells expressing $KRAS^{G12V}$ compared to parental NIH 3T3 cells expressing $KRAS^{G12V}$, further demonstrating a requirement for AGO2 in KRAS-driven transformation (Figure 7C, lower panel). At the protein level, NIH 3T3 *AGO2*−/− cells stably expressing $KRAS^{G12V}$ showed reduced expression of mutant KRAS compared to that of NIH 3T3 cells stably expressing $KRAS^{G12V}$ (Figure 7D). Reduced activation of phospho-Akt signaling by mutant KRAS and a slight increase in phospho-ERK signaling in NIH 3T3 AGO2−/− cells suggests that AGO2 plays an essential role in modulating the signaling output of mutant KRAS.

Taken together, we have established AGO2 as a critical regulator of RAS-GTP in cells, and our study posits an essential role for the KRAS-AGO2 interaction in oncogenic KRAS-driven cellular transformation.

DISCUSSION

RAS, one of the first proto-oncogenes identified (DeFeo et al., 1981), has emerged as one of the genes with most-frequent recurrent mutations in a broad spectrum of human cancers. In recent years, there is a renewed interest in targeting RAS to alter its status from an undruggable to druggable candidate (Burns et al., 2014; Ostrem et al., 2013; Spiegel et al., 2014; Stephen et al., 2014; Sun et al., 2012). In this context, discovery of novel endogenous interactors of RAS could potentially advance our understanding of RAS biology and provide additional therapeutic avenues.

Here, we identify the interaction of RAS with AGO2, a key mediator of RNA-based gene silencing (Czech and Hannon, 2011; Peters and Meister, 2007; Wilson and Doudna, 2013). Like guanine nucleotide exchange factors (GEFs), AGO2 binds RAS-GTP and RAS-GDP and likely interacts functionally with both wild-type and oncogenic RAS proteins (Jeng et al., 2012; Margarit et al., 2003). Furthermore, AGO2 and RAS co-localize in the ER, known sites for both RAS trafficking and AGO2 RISC activity. The KRAS-AGO2 interaction involves Y64 in the Switch II domain of KRAS and K112-E114 residues in the N-terminal Wedge domain of AGO2 (Figure 7E). Functionally, the mutant KRAS-AGO2 interaction is critical for KRAS-mediated oncogenesis. Mechanistically, mutant KRAS binding attenuates AGO2 N-terminal-dependent microRNA duplex unwinding, critical for functional RISC assembly. Reciprocally, AGO2 modulates mutant-KRAS-mediated signaling output, particularly the AKT-mTOR pathway.

Our study focused on analyzing endogenous interactors of RAS, common across a panel of cancer cells spanning the spectrum of KRAS aberrations. To the best of our knowledge, this is the first study using endogenous RAS as bait for mass spectrometric analyses, as all previous coIP MS analyses used N-terminal epitope-tagged *HRAS*, *MRAS*, or *RRAS* ectopically expressed in NIH 3T3 cells (Goldfinger et al., 2007; Vasilescu et al., 2004). Studies using tagged AGO2 as bait for mass spectrometry have also been reported (MacRae et al., 2008; Meister et al., 2005) and, as a 25-kDa cutoff was employed for analyses, may have missed the detection of the 21 kDa RAS protein. In this study, the pull-down of AGO2 using multiple independent antibodies consistently co-precipitated RAS (Figure 1C), and we found that this interaction is direct, as assessed using purified components (Figure 4). Endogenously, the RAS-AGO2 interaction is readily detected in both cancer and benign cells, independent of *KRAS* mutation status (Figure 1D), portending a fundamental role for this interaction in the cell.

KRAS interacts with AGO2 through the Switch II domain, the Y64 residue being critical for its AGO2 association. The

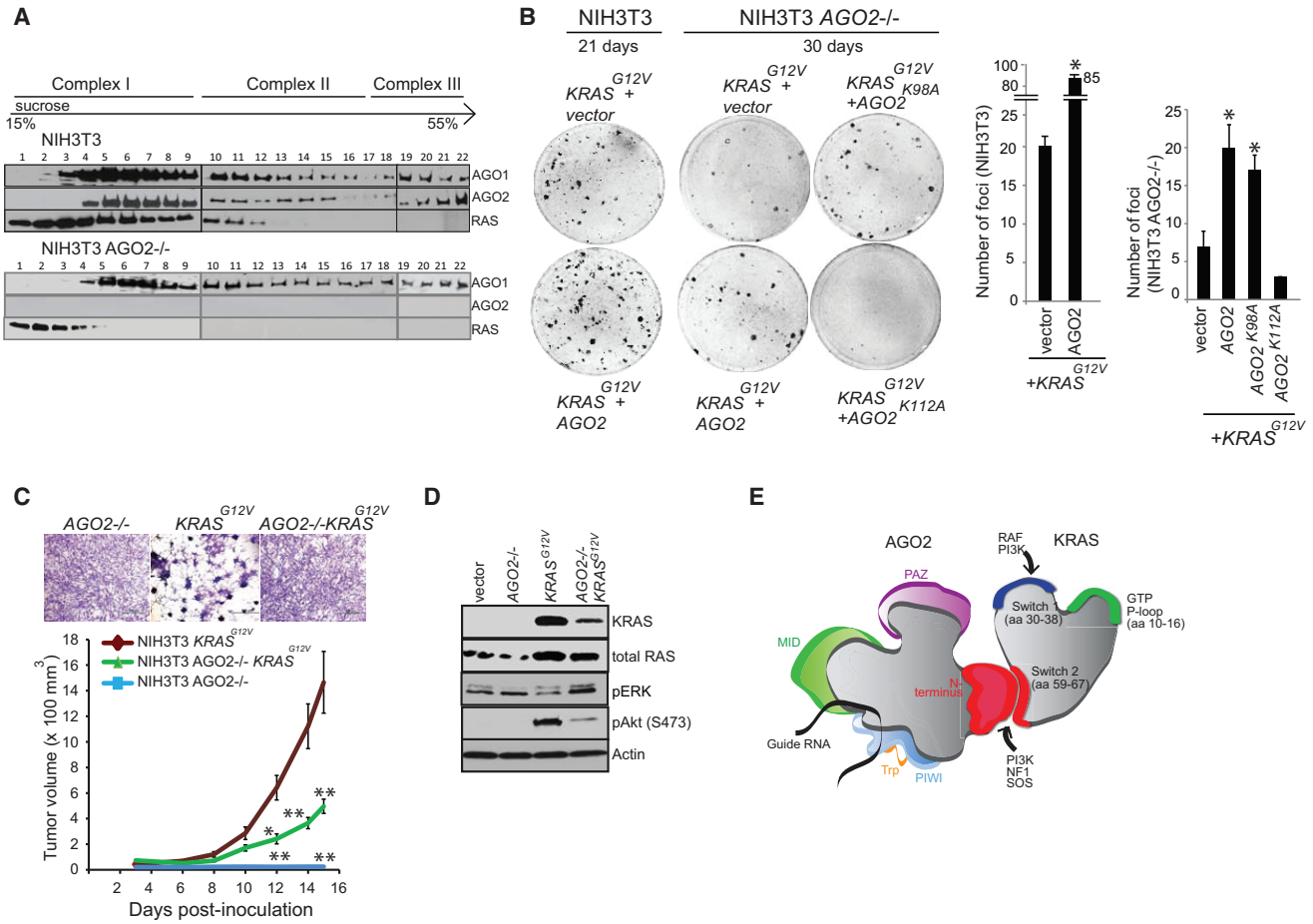

Figure 7. AGO2 Interaction Is Required for Maximal Oncogenic Potential of Mutant KRAS

(A) Sucrose density gradient fractionation of parental NIH 3T3, NIH 3T3 *KRAS*^{G12V}, and NIH 3T3 *AGO2*−/− cell lysates followed by immunoblot detection of RAS, AGO1, and AGO2 proteins.

(B) (Left) Representative images of *KRAS*^{G12V}-driven foci in NIH 3T3 and NIH 3T3 *AGO2*−/− cells upon co-transfection with various *AGO2* constructs. (Right) Quantitation of foci from two replicate experiments is shown. Error bars show SEM, and asterisks indicate p values less than 0.005 for the indicated conditions compared to vector control.

(C) Upper panel shows crystal violet staining of indicated stable lines grown in 10% serum. (Lower panel) In vivo growth of NIH 3T3 or NIH 3T3 *AGO2*−/− cells stably expressing *KRAS*^{G12V} in nude mice is shown. For each group (n = 8), 500,000 cells were injected and average tumor volume (in mm^3) was plotted on y axis and days after injection on the x axis. Error bars are SEM. *p < 0.05 and **p < 0.005 at the indicated times.

(D) Immunoblot analysis showing reduced expression of oncogenic KRAS in *KRAS AGO2*−/− stably expressing *KRAS*^{G12V} and the extent of phospho-ERK and phospho-AKT activation in these cells.

(E) Schematic representation of the N-terminal domain of AGO2 interacting with the Switch II domain in RAS.

See also Figure S7.

Switch II domain and particularly Y64 was recently demonstrated to be critical in hematopoietic malignancies, where *KRAS*^{G12DY64G} mutant expressed at lower levels compared to *KRAS*^{G12D} (Shieh et al., 2013), much like we observed in our NIH 3T3 model, extending a role for the KRAS-AGO2 interaction in models other than lung and pancreas. It should be noted that the Switch II domain in RAS is the site for allosteric regulation through its binding to various regulators and may contribute to the biological effects observed in these studies. Yet, this study provides a first instance where the mutant KRAS Switch II domain (and Y64) has a direct bearing on RISC assembly through its association with AGO2.

The AGO2 N-terminal domain represents the most-distinct region in the highly conserved AGO protein family. A recent report (Kwak and Tomari, 2012) suggests that the region we identified in AGO2 as critical for RAS binding (i.e., the "wedge domain") is important for small RNA duplex unwinding, a prerequisite for RISC assembly. Using isogenic lines, we demonstrate that mutant KRAS, but not wild-type KRAS, interaction with AGO2 attenuates microRNA duplex unwinding function with a direct bearing on AGO2-RISC assembly. Inhibition of RISC assembly by mutant KRAS may be the critical step that likely contributes to global loss of microRNA levels and downstream effects on increased protein translation of target mRNAs, features of

human tumors (Lu et al., 2005). Because we have used mutant KRAS constructs that do not have 3′ UTR regions that can bind microRNAs, it remains unclear how AGO2 elevates mutant KRAS levels (Figures 5A and 6B) to increase its transformation potential.

Recent studies have shown that KRAS, but not HRAS, translation is tightly regulated by rare synonymous codons of the *KRAS* transcript (Lampson et al., 2013; Pershing et al., 2015), suggesting a significant role for KRAS regulation at a level prior to its better-characterized post-translational modifications. An association of mutant KRAS with the RNA machinery through binding to HNRNPA2B1 was also reported (Barceló et al., 2014), supporting a likely interface of RAS with the RNA-processing machinery, including the hub protein AGO2 as observed in our study. The EGFR kinase was also recently shown to phosphorylate AGO2 in response to hypoxia, leading to inhibition of AGO2-mediated microRNA processing (McCarthy, 2013; Shen et al., 2013). Similarly, Akt was shown to phosphorylate AGO2 to inhibit *AGO2*-mediated mRNA endonucleolytic activity (Horman et al., 2013). Interestingly, AGO2 phosphorylation also leads to inhibition of microRNA loading into RISC complexes in the presence of mutant $HRAS^{G12V}$ (Yang et al., 2014). The identification of AGO2 as a critical partner of RAS further provides a direct mechanistic link between RAS oncogenic signaling and RNA silencing. Further illumination of such integral effector mechanisms of RAS may inform novel approaches to therapeutically target this frequently mutated cancer pathway.

EXPERIMENTAL PROCEDURES

Co-immunoprecipitation and Tandem Mass Spectrometric Analysis

Methods used for immunoprecipitation with RAS/control IgG followed by tandem mass spectrometric analysis and database searching are schematically outlined in Figure S1D. Complete data of the peptides represented in the RAS coIP mass spectrometric analysis from the different cell lines are provided in Table S5.

Immunoprecipitation and Western Blot Analysis

Routine methods to immunoprecipitate proteins were employed and detailed in the Supplemental Experimental Procedures. Antibodies used in the study are detailed in Table S3.

RAS-GTP Pull-Down Assay

The RAS-RAF interaction was studied using the RBD agarose beads as per manufacturer's instructions (Millipore) and detailed in the Supplemental Experimental Procedures.

Focus Formation Assay

Foci formation assays were performed by transfecting/co-transfecting (the indicated constructs) 150,000 early passage NIH 3T3 cells in 6-well dishes using Fugene HD (Promega). After 2 days, cells were trypsinized and plated onto 150 mm dishes containing 4%–5% calf serum. The cells were maintained under low serum conditions, and medium was refreshed every 2 days. After 21 days in culture, the plates were stained for foci using crystal violet.

Generation of NIH 3T3 *AGO2*−/− Line

AGO2-knockout NIH 3T3 cells were generated by CRISPR-Cas9-mediated genome engineering (Ran et al., 2013). Genomic regions in murine AGO2 between exons 8 and 9 and between exons 11and 12 were targeted for deletion using primers TCCTTGGTTACCCGATCCTGG and AGAGACTATCTG CAACTATGG, respectively (PAM motif underlined). Selection of clones is detailed in the Supplemental Experimental Procedures.

iSHiRLoC Analyses

Oligos (*let-7*-a1 guide: P-UGA GGU AGU AGG UUG UAU AGU U-X Cy5, where X = Cy3 or Cy5; *let-7*-a1-passenger: P-CUA UAC AAU CUA CUG UCU UUC C-Y, where Y = OH, Cy3, or Cy5) were microinjected in cells and incubated in phenol red-free DMEM containing 2% (v/v) CS in the presence of a 5% CO_2 atmosphere at 37°C for the indicated amounts of time prior to imaging. Details of microinjection and imaging are provided in the Supplemental Experimental Procedures.

Extract Preparation and In Vitro miRNA Unwinding Assay

Cell extracts were prepared as described (Kwak and Tomari, 2012; Rakotondrafara and Hentze, 2011), with minor modifications detailed in Supplemental Experimental Procedures.

Further details on other methods are provided in the Supplemental Experimental Procedures.

Xenograft Studies

All experimental procedures involving mice were approved by the University Committee on Use and Care of Animals at the University of Michigan and conform to their relevant regulatory standards and are detailed in the Supplemental Experimental Procedures.

SUPPLEMENTAL INFORMATION

Supplemental Information includes Supplemental Experimental Procedures, seven figures, and five tables and can be found with this article online at http://dx.doi.org/10.1016/j.celrep.2016.01.034.

AUTHOR CONTRIBUTIONS

S.S. performed RAS/AGO2 immunoprecipitation, in vitro binding, cellular fractionation, immunoblot analyses, RAS/AGO2 knockdown, and overexpression cell-biology-based experiments. S.S. jointly conceived the study with C.K.-S. and A.M.C. *let-7*-based assays were carried out by S.P.; immunofluorescence analyses by S.P. and R.M.; sucrose density fractionation by R.M.; cloning and construct generation by V.K.; NIH3T3 *AGO2*−/− cells using CRISPR/Cas9 by Y.H.; IP-mass spectrometric analysis by A.K.Y.; experimental assistance and replication of studies by H.G.; microRNA sequencing and analysis by X.C. and S.M.D.; recombinant protein preparation and purification by J.A.S.; KRAS reagents and advice on KRAS biology by Y.W., A.F., K.S., and G.B.; single molecule analysis by S.P. and N.G.W.; manuscript preparation by S.S., C.K.-S., and A.M.C.; and funding and overall supervision of the study by A.M.C.

ACKNOWLEDGMENTS

We acknowledge the work of Shanker Kalyan-Sundaram, Krishnapriya Chinnaswamy, Vijaya L. Dommeti, Matthew Shuler, Anton Poliakov, Xiaoju Wang, and Vishalakshi Krishnan, who helped with analysis and experimentation. We thank Phillip Zamore for providing AGO2−/− and AGO2−/− + AGO2 MEFs and Mariano Barbacid for providing KRAS-only-expressing MEFs. We thank Eric Fearon for helpful discussions; Joseph Mierzwa, Kevin Eid, and Jincheng Pan for technical assistance; Bushra Ateeq and Rachell Stender for help with the xenograft studies; William Brown for His-AGO2 protein preparation; and Robin Kunkel for assistance with schematic representations. We also thank Ingrid Apel, Xiaojun Jing, and David O. Apiyo (Pall Life Sciences) for carrying out additional experiments that were not used for the final manuscript. We also benefited from discussions with Denzil Bernard (structure-function) and John O'Bryan (University of Illinois; nucleotide loading). We thank Ester Fernandez-Salas for her inputs on the manuscript. We thank the University of Michigan Xenograft Core and Dr. Diane Simeone for providing PDX1319 cell line. S.P. was supported by IFOM Fondazione Istituto FIRC di Oncologia Molecolare, Milan, Italy (sponsor: Fabrizio D'Adda di Fagagna). R.M. is supported by Prostate Cancer Foundation Young Investigator Award. Y.W. was supported by a Howard Hughes Medical Institute (HHMI) Medical Student Research Fellowship. and A.F. by a Damon Runyon Foundation Fellowship. A.M.C. is supported by the Alfred A. Taubman Institute and the HHMI.

A.M.C. and K.S. are American Cancer Society Research Professors. This project is supported in part by NIH grants NIH 1R21 AI109791 (PI: N.G.W.), RO1 CA154365 and R37 CA40046, and the Prostate Cancer Foundation (PI: A.M.C.).

Received: December 17, 2014
Revised: December 17, 2015
Accepted: January 7, 2016
Published: February 4, 2016

REFERENCES

Baines, A.T., Xu, D., and Der, C.J. (2011). Inhibition of Ras for cancer treatment: the search continues. Future Med. Chem. *3*, 1787–1808.

Balmain, A., and Pragnell, I.B. (1983). Mouse skin carcinomas induced in vivo by chemical carcinogens have a transforming Harvey-ras oncogene. Nature *303*, 72–74.

Barceló, C., Etchin, J., Mansour, M.R., Sanda, T., Ginesta, M.M., Sanchez-Arévalo Lobo, V.J., Real, F.X., Capellà, G., Estanyol, J.M., Jaumot, M., et al. (2014). Ribonucleoprotein HNRNPA2B1 interacts with and regulates oncogenic KRAS in pancreatic ductal adenocarcinoma cells. Gastroenterology *147*, 882–892.e8.

Benhamed, M., Herbig, U., Ye, T., Dejean, A., and Bischof, O. (2012). Senescence is an endogenous trigger for microRNA-directed transcriptional gene silencing in human cells. Nat. Cell Biol. *14*, 266–275.

Bivona, T.G., Quatela, S.E., Bodemann, B.O., Ahearn, I.M., Soskis, M.J., Mor, A., Miura, J., Wiener, H.H., Wright, L., Saba, S.G., et al. (2006). PKC regulates a farnesyl-electrostatic switch on K-Ras that promotes its association with Bcl-XL on mitochondria and induces apoptosis. Mol. Cell *21*, 481–493.

Brenner, J.C., Ateeq, B., Li, Y., Yocum, A.K., Cao, Q., Asangani, I.A., Patel, S., Wang, X., Liang, H., Yu, J., et al. (2011). Mechanistic rationale for inhibition of poly(ADP-ribose) polymerase in ETS gene fusion-positive prostate cancer. Cancer Cell *19*, 664–678.

Broderick, J.A., Salomon, W.E., Ryder, S.P., Aronin, N., and Zamore, P.D. (2011). Argonaute protein identity and pairing geometry determine cooperativity in mammalian RNA silencing. RNA *17*, 1858–1869.

Burns, M.C., Sun, Q., Daniels, R.N., Camper, D., Kennedy, J.P., Phan, J., Olejniczak, E.T., Lee, T., Waterson, A.G., Rossanese, O.W., and Fesik, S.W. (2014). Approach for targeting Ras with small molecules that activate SOS-mediated nucleotide exchange. Proc. Natl. Acad. Sci. USA *111*, 3401–3406.

Cao, Q., Wang, X., Zhao, M., Yang, R., Malik, R., Qiao, Y., Poliakov, A., Yocum, A.K., Li, Y., Chen, W., et al. (2014). The central role of EED in the orchestration of polycomb group complexes. Nat. Commun. *5*, 3127.

Cheng, C.M., Li, H., Gasman, S., Huang, J., Schiff, R., and Chang, E.C. (2011). Compartmentalized Ras proteins transform NIH 3T3 cells with different efficiencies. Mol. Cell. Biol. *31*, 983–997.

Cichowski, K., and Jacks, T. (2001). NF1 tumor suppressor gene function: narrowing the GAP. Cell *104*, 593–604.

COSMIC (2013). Catalog of Somatic Mutations in Cancer, COSMIC Release v66 (Wellcome Trust Sanger Institute).

Cox, A.D., and Der, C.J. (2010). Ras history: The saga continues. Small GTPases *1*, 2–27.

Czech, B., and Hannon, G.J. (2011). Small RNA sorting: matchmaking for Argonautes. Nat. Rev. Genet. *12*, 19–31.

DeFeo, D., Gonda, M.A., Young, H.A., Chang, E.H., Lowy, D.R., Scolnick, E.M., and Ellis, R.W. (1981). Analysis of two divergent rat genomic clones homologous to the transforming gene of Harvey murine sarcoma virus. Proc. Natl. Acad. Sci. USA *78*, 3328–3332.

Diederichs, S., and Haber, D.A. (2007). Dual role for argonautes in microRNA processing and posttranscriptional regulation of microRNA expression. Cell *131*, 1097–1108.

Downward, J. (2003). Targeting RAS signalling pathways in cancer therapy. Nat. Rev. Cancer *3*, 11–22.

Drosten, M., Dhawahir, A., Sum, E.Y., Urosevic, J., Lechuga, C.G., Esteban, L.M., Castellano, E., Guerra, C., Santos, E., and Barbacid, M. (2010). Genetic analysis of Ras signalling pathways in cell proliferation, migration and survival. EMBO J. *29*, 1091–1104.

Dudley, N.R., and Goldstein, B. (2003). RNA interference: silencing in the cytoplasm and nucleus. Curr. Opin. Mol. Ther. *5*, 113–117.

Gagnon, K.T., Li, L., Chu, Y., Janowski, B.A., and Corey, D.R. (2014). RNAi factors are present and active in human cell nuclei. Cell Rep. *6*, 211–221.

Goldfinger, L.E., Ptak, C., Jeffery, E.D., Shabanowitz, J., Han, J., Haling, J.R., Sherman, N.E., Fox, J.W., Hunt, D.F., and Ginsberg, M.H. (2007). An experimentally derived database of candidate Ras-interacting proteins. J. Proteome Res. *6*, 1806–1811.

Gysin, S., Salt, M., Young, A., and McCormick, F. (2011). Therapeutic strategies for targeting ras proteins. Genes Cancer *2*, 359–372.

Hand, P.H., Thor, A., Wunderlich, D., Muraro, R., Caruso, A., and Schlom, J. (1984). Monoclonal antibodies of predefined specificity detect activated ras gene expression in human mammary and colon carcinomas. Proc. Natl. Acad. Sci. USA *81*, 5227–5231.

Höck, J., Weinmann, L., Ender, C., Rüdel, S., Kremmer, E., Raabe, M., Urlaub, H., and Meister, G. (2007). Proteomic and functional analysis of Argonaute-containing mRNA-protein complexes in human cells. EMBO Rep. *8*, 1052–1060.

Horman, S.R., Janas, M.M., Litterst, C., Wang, B., MacRae, I.J., Sever, M.J., Morrissey, D.V., Graves, P., Luo, B., Umesalma, S., et al. (2013). Akt-mediated phosphorylation of argonaute 2 downregulates cleavage and upregulates translational repression of MicroRNA targets. Mol. Cell *50*, 356–367.

Jeng, H.H., Taylor, L.J., and Bar-Sagi, D. (2012). Sos-mediated cross-activation of wild-type Ras by oncogenic Ras is essential for tumorigenesis. Nat. Commun. *3*, 1168.

Johnson, S.M., Grosshans, H., Shingara, J., Byrom, M., Jarvis, R., Cheng, A., Labourier, E., Reinert, K.L., Brown, D., and Slack, F.J. (2005). RAS is regulated by the let-7 microRNA family. Cell *120*, 635–647.

Karachaliou, N., Mayo, C., Costa, C., Magrí, I., Gimenez-Capitan, A., Molina-Vila, M.A., and Rosell, R. (2013). KRAS mutations in lung cancer. Clin. Lung Cancer *14*, 205–214.

Karnoub, A.E., and Weinberg, R.A. (2008). Ras oncogenes: split personalities. Nat. Rev. Mol. Cell Biol. *9*, 517–531.

Kim, Y.J., Maizel, A., and Chen, X. (2014). Traffic into silence: endomembranes and post-transcriptional RNA silencing. EMBO J. *33*, 968–980.

Kwak, P.B., and Tomari, Y. (2012). The N domain of Argonaute drives duplex unwinding during RISC assembly. Nat. Struct. Mol. Biol. *19*, 145–151.

Lampson, B.L., Pershing, N.L., Prinz, J.A., Lacsina, J.R., Marzluff, W.F., Nicchitta, C.V., MacAlpine, D.M., and Counter, C.M. (2013). Rare codons regulate KRas oncogenesis. Curr. Biol. *23*, 70–75.

Lauchle, J.O., Braun, B.S., Loh, M.L., and Shannon, K. (2006). Inherited predispositions and hyperactive Ras in myeloid leukemogenesis. Pediatr. Blood Cancer *46*, 579–585.

Lee, Y.S., and Dutta, A. (2007). The tumor suppressor microRNA let-7 represses the HMGA2 oncogene. Genes Dev. *21*, 1025–1030.

Löhr, M., Klöppel, G., Maisonneuve, P., Lowenfels, A.B., and Lüttges, J. (2005). Frequency of K-ras mutations in pancreatic intraductal neoplasias associated with pancreatic ductal adenocarcinoma and chronic pancreatitis: a meta-analysis. Neoplasia *7*, 17–23.

Lu, J., Getz, G., Miska, E.A., Alvarez-Saavedra, E., Lamb, J., Peck, D., Sweet-Cordero, A., Ebert, B.L., Mak, R.H., Ferrando, A.A., et al. (2005). MicroRNA expression profiles classify human cancers. Nature *435*, 834–838.

MacRae, I.J., Ma, E., Zhou, M., Robinson, C.V., and Doudna, J.A. (2008). In vitro reconstitution of the human RISC-loading complex. Proc. Natl. Acad. Sci. USA *105*, 512–517.

Margarit, S.M., Sondermann, H., Hall, B.E., Nagar, B., Hoelz, A., Pirruccello, M., Bar-Sagi, D., and Kuriyan, J. (2003). Structural evidence for feedback

activation by Ras.GTP of the Ras-specific nucleotide exchange factor SOS. Cell *112*, 685–695.

McCarthy, N. (2013). MicroRNA: lacking in maturity. Nat. Rev. Cancer *13*, 377.

Meister, G., Landthaler, M., Peters, L., Chen, P.Y., Urlaub, H., Lührmann, R., and Tuschl, T. (2005). Identification of novel argonaute-associated proteins. Curr. Biol. *15*, 2149–2155.

Ostrem, J.M., Peters, U., Sos, M.L., Wells, J.A., and Shokat, K.M. (2013). K-Ras(G12C) inhibitors allosterically control GTP affinity and effector interactions. Nature *503*, 548–551.

Paroo, Z., Ye, X., Chen, S., and Liu, Q. (2009). Phosphorylation of the human microRNA-generating complex mediates MAPK/Erk signaling. Cell *139*, 112–122.

Pershing, N.L., Lampson, B.L., Belsky, J.A., Kaltenbrun, E., MacAlpine, D.M., and Counter, C.M. (2015). Rare codons capacitate Kras-driven de novo tumorigenesis. J. Clin. Invest. *125*, 222–233.

Peters, L., and Meister, G. (2007). Argonaute proteins: mediators of RNA silencing. Mol. Cell *26*, 611–623.

Pitchiaya, S., Androsavich, J.R., and Walter, N.G. (2012). Intracellular single molecule microscopy reveals two kinetically distinct pathways for microRNA assembly. EMBO Rep. *13*, 709–715.

Pitchiaya, S., Krishnan, V., Custer, T.C., and Walter, N.G. (2013). Dissecting non-coding RNA mechanisms in cellulo by Single-molecule High-Resolution Localization and Counting. Methods *63*, 188–199.

Prior, I.A., and Hancock, J.F. (2012). Ras trafficking, localization and compartmentalized signalling. Semin. Cell Dev. Biol. *23*, 145–153.

Pylayeva-Gupta, Y., Grabocka, E., and Bar-Sagi, D. (2011). RAS oncogenes: weaving a tumorigenic web. Nat. Rev. Cancer *11*, 761–774.

Qiu, R.G., Chen, J., Kirn, D., McCormick, F., and Symons, M. (1995). An essential role for Rac in Ras transformation. Nature *374*, 457–459.

Rakotondrafara, A.M., and Hentze, M.W. (2011). An efficient factor-depleted mammalian in vitro translation system. Nat. Protoc. *6*, 563–571.

Ran, F.A., Hsu, P.D., Wright, J., Agarwala, V., Scott, D.A., and Zhang, F. (2013). Genome engineering using the CRISPR-Cas9 system. Nat. Protoc. *8*, 2281–2308.

Rüdel, S., Flatley, A., Weinmann, L., Kremmer, E., and Meister, G. (2008). A multifunctional human Argonaute2-specific monoclonal antibody. RNA *14*, 1244–1253.

Rüdel, S., Wang, Y., Lenobel, R., Körner, R., Hsiao, H.H., Urlaub, H., Patel, D., and Meister, G. (2011). Phosphorylation of human Argonaute proteins affects small RNA binding. Nucleic Acids Res. *39*, 2330–2343.

Schubbert, S., Shannon, K., and Bollag, G. (2007). Hyperactive Ras in developmental disorders and cancer. Nat. Rev. Cancer *7*, 295–308.

Shaw, R.J., and Cantley, L.C. (2006). Ras, PI(3)K and mTOR signalling controls tumour cell growth. Nature *441*, 424–430.

Shen, J., Xia, W., Khotskaya, Y.B., Huo, L., Nakanishi, K., Lim, S.O., Du, Y., Wang, Y., Chang, W.C., Chen, C.H., et al. (2013). EGFR modulates microRNA maturation in response to hypoxia through phosphorylation of AGO2. Nature *497*, 383–387.

Shieh, A., Ward, A.F., Donlan, K.L., Harding-Theobald, E.R., Xu, J., Mullighan, C.G., Zhang, C., Chen, S.C., Su, X., Downing, J.R., et al. (2013). Defective K-Ras oncoproteins overcome impaired effector activation to initiate leukemia in vivo. Blood *121*, 4884–4893.

Shih, C., Padhy, L.C., Murray, M., and Weinberg, R.A. (1981). Transforming genes of carcinomas and neuroblastomas introduced into mouse fibroblasts. Nature *290*, 261–264.

Spiegel, J., Cromm, P.M., Zimmermann, G., Grossmann, T.N., and Waldmann, H. (2014). Small-molecule modulation of Ras signaling. Nat. Chem. Biol. *10*, 613–622.

Stalder, L., Heusermann, W., Sokol, L., Trojer, D., Wirz, J., Hean, J., Fritzsche, A., Aeschimann, F., Pfanzagl, V., Basselet, P., et al. (2013). The rough endoplasmatic reticulum is a central nucleation site of siRNA-mediated RNA silencing. EMBO J. *32*, 1115–1127.

Stephen, A.G., Esposito, D., Bagni, R.K., and McCormick, F. (2014). Dragging ras back in the ring. Cancer Cell *25*, 272–281.

Sun, Q., Burke, J.P., Phan, J., Burns, M.C., Olejniczak, E.T., Waterson, A.G., Lee, T., Rossanese, O.W., and Fesik, S.W. (2012). Discovery of small molecules that bind to K-Ras and inhibit Sos-mediated activation. Angew. Chem. Int. Ed. Engl. *51*, 6140–6143.

Sweet, R.W., Yokoyama, S., Kamata, T., Feramisco, J.R., Rosenberg, M., and Gross, M. (1984). The product of ras is a GTPase and the T24 oncogenic mutant is deficient in this activity. Nature *311*, 273–275.

Symonds, J.M., Ohm, A.M., Carter, C.J., Heasley, L.E., Boyle, T.A., Franklin, W.A., and Reyland, M.E. (2011). Protein kinase C δ is a downstream effector of oncogenic K-ras in lung tumors. Cancer Res. *71*, 2087–2097.

Trahey, M., and McCormick, F. (1987). A cytoplasmic protein stimulates normal N-ras p21 GTPase, but does not affect oncogenic mutants. Science *238*, 542–545.

Vasilescu, J., Guo, X., and Kast, J. (2004). Identification of protein-protein interactions using in vivo cross-linking and mass spectrometry. Proteomics *4*, 3845–3854.

Wang, B., Li, S., Qi, H.H., Chowdhury, D., Shi, Y., and Novina, C.D. (2009). Distinct passenger strand and mRNA cleavage activities of human Argonaute proteins. Nat. Struct. Mol. Biol. *16*, 1259–1266.

Wilson, R.C., and Doudna, J.A. (2013). Molecular mechanisms of RNA interference. Annu. Rev. Biophys. *42*, 217–239.

Yang, M., Haase, A.D., Huang, F.K., Coulis, G., Rivera, K.D., Dickinson, B.C., Chang, C.J., Pappin, D.J., Neubert, T.A., Hannon, G.J., et al. (2014). Dephosphorylation of tyrosine 393 in argonaute 2 by protein tyrosine phosphatase 1B regulates gene silencing in oncogenic RAS-induced senescence. Mol. Cell *55*, 782–790.

Zeng, Y., Sankala, H., Zhang, X., and Graves, P.R. (2008). Phosphorylation of Argonaute 2 at serine-387 facilitates its localization to processing bodies. Biochem. J. *413*, 429–436.

Cell Reports, Volume *14*

Supplemental Information

KRAS Engages AGO2 to Enhance Cellular Transformation

Sunita Shankar, Sethuramasundaram Pitchiaya, Rohit Malik, Vishal Kothari, Yasuyuki Hosono, Anastasia K. Yocum, Harika Gundlapalli, Yasmine White, Ari Firestone, Xuhong Cao, Saravana M. Dhanasekaran, Jeanne A. Stuckey, Gideon Bollag, Kevin Shannon, Nils G. Walter, Chandan Kumar-Sinha, and Arul M. Chinnaiyan

Figure S1

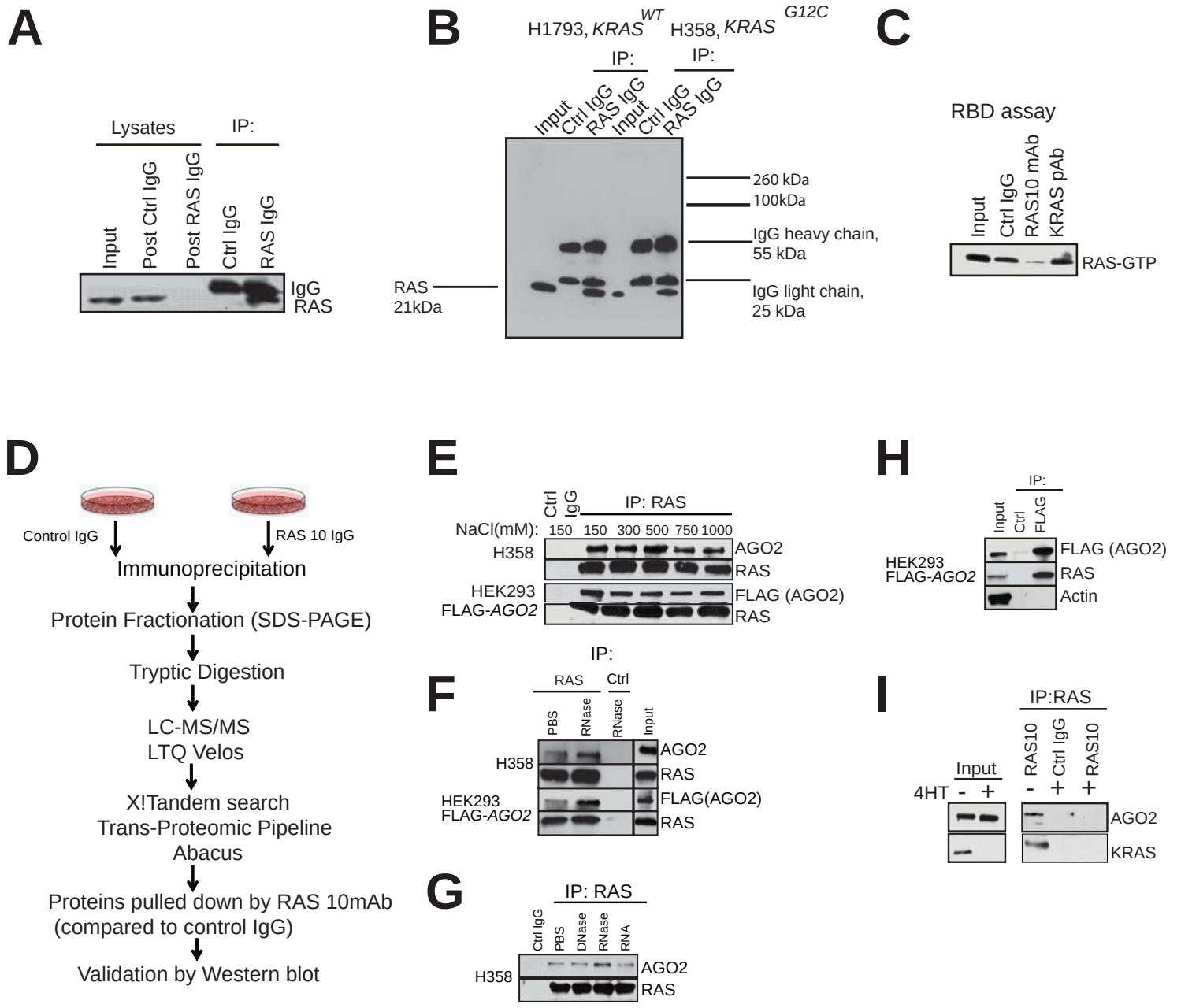
A
Lysates
IP:
Input
Post Ctrl IgG
Post RAS IgG
Ctrl IgG
RAS IgG
IgG
RAS
B
H1793, KRAS WT
H358, KRAS G12C
IP:
IP:
Input
Ctrl IgG
RAS IgG
Input
Ctrl IgG
RAS IgG
260 kDa
100kDa
IgG heavy chain, 55 kDa
IgG light chain, 25 kDa
RAS 21kDa
C
RBD assay
Input
Ctrl IgG
RAS10 mAb
KRAS pAb
RAS-GTP
D
Control IgG
RAS 10 IgG
Immunoprecipitation
Protein Fractionation (SDS-PAGE)
Tryptic Digestion
LC-MS/MS
LTQ Velos
X!Tandem search
Trans-Proteomic Pipeline
Abacus
Proteins pulled down by RAS 10mAb
(compared to control IgG)
Validation by Western blot
E
Ctrl IgG
IP: RAS
NaCl(mM): 150 150 300 500 750 1000
H358
AGO2
RAS
HEK293
FLAG-AGO2
FLAG (AGO2)
RAS
F
IP:
RAS
Ctrl
PBS
RNase
RNase
Input
H358
AGO2
RAS
HEK293
FLAG-AGO2
FLAG(AGO2)
RAS
G
IP: RAS
Ctrl IgG
PBS
DNase
RNase
RNA
H358
AGO2
RAS
H
IP:
Input
Ctrl
FLAG
HEK293
FLAG-AGO2
FLAG (AGO2)
RAS
Actin
I
IP:RAS
Input
4HT - +
RAS10
- +
Ctrl IgG
+
RAS10
+
AGO2
KRAS

Figure S1. Related to Figure 1. Characterization of RAS10 mAb, used for mass spectrometric identification of RAS-AGO2 interaction, validated by immunoblot analysis in the presence of RNAse. (A) Efficiency of the RAS10 mAb in pulling down RAS as seen by immunoblot analysis of RAS immunoprecipitates. The RAS10 mAb was used for both immunoprecipitation (IP) and immunoblot (IB) analysis. **(B)** Scan of the entire immunoblot using the RAS10 mAb demonstrating the specificity of detection using total cell lysates or immunoprecipitates. Both the IP and immunoblotting were performed using the RAS10 mAb. **(C)** Immunoblot analysis of RAS bound to RAS binding domain of RAF (RBD) in the presence of different RAS antibodies. RBD agarose beads were added to H358 cell lysates in the presence of RAS10 monoclonal or KRAS polyclonal (KRAS sc-521) antibody. Reduced interaction between RAS-GTP and RBD in the presence of RAS10 antibody indicates that the antibody binds the RAS Switch I domain and interferes with the RAS-RAF interaction. KRAS sc-521 polyclonal antibody, which binds the C-terminal region of KRAS was used as control. RAS10 mAb was used for IB analysis. **(D)** Schematic of the methodology used for RAS Co-IP MS. Proteins pulled down by the corresponding isotypic control IgG in each cell line were considered as non-specific hits and were excluded from the data obtained from RAS IP. (**E**) IP of RAS in H358 and HEK293 FLAG-*AGO2* expressing cells under increasing concentrations of salt followed by immunoblot analysis. Immunoblot analysis of RAS10 Ab immunoprecipitates from H358 lung cancer (endogenous) and FLAG-*AGO2* overexpressing HEK293 cell lysates treated with RNase (**F**) and DNase (**G**). RAS10 mAb was used for both IP and IB. RAS10 mAb was used for both IP and IB. (**H**) FLAG tagged AGO2 expressed in HEK293 immunoprecipitates RAS. Actin was used as control. (**I**) Co-IP analysis in RASless MEFs demonstrates specificity of RAS-AGO2 interaction. Genetically engineered mouse embryonic fibroblasts expressing KRAS were treated with 4-hydroxytamoxifen prior to co-IP using RAS10 antibody. Immunoblot analysis shows tamoxifen treated RASless MEFs abrogate KRAS expression and fail to immunoprecipitate AGO2.

Figure S2

A

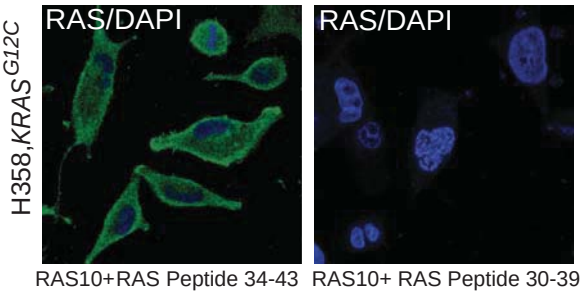

B

Organelle	Region	Blue / Green	Blue / Red	Green / Red
Mitochondria	I	0.34	0.15	0.06
	II	0.17	0.45	0.20
	III	0.04	0.04	0.19
Golgi	I	0.36	0.20	0.17
	II	0.20	0.30	0.35
	III	0.37	0.27	0.17
Endosomes	I	0.31	0.30	0.17
	II	0.30	0.47	0.18
	III	0.14	0.23	0.11
ER	I	0.62	0.53	0.62
	II	0.21	0.35	0.15
	III	0.53	0.58	0.58

C

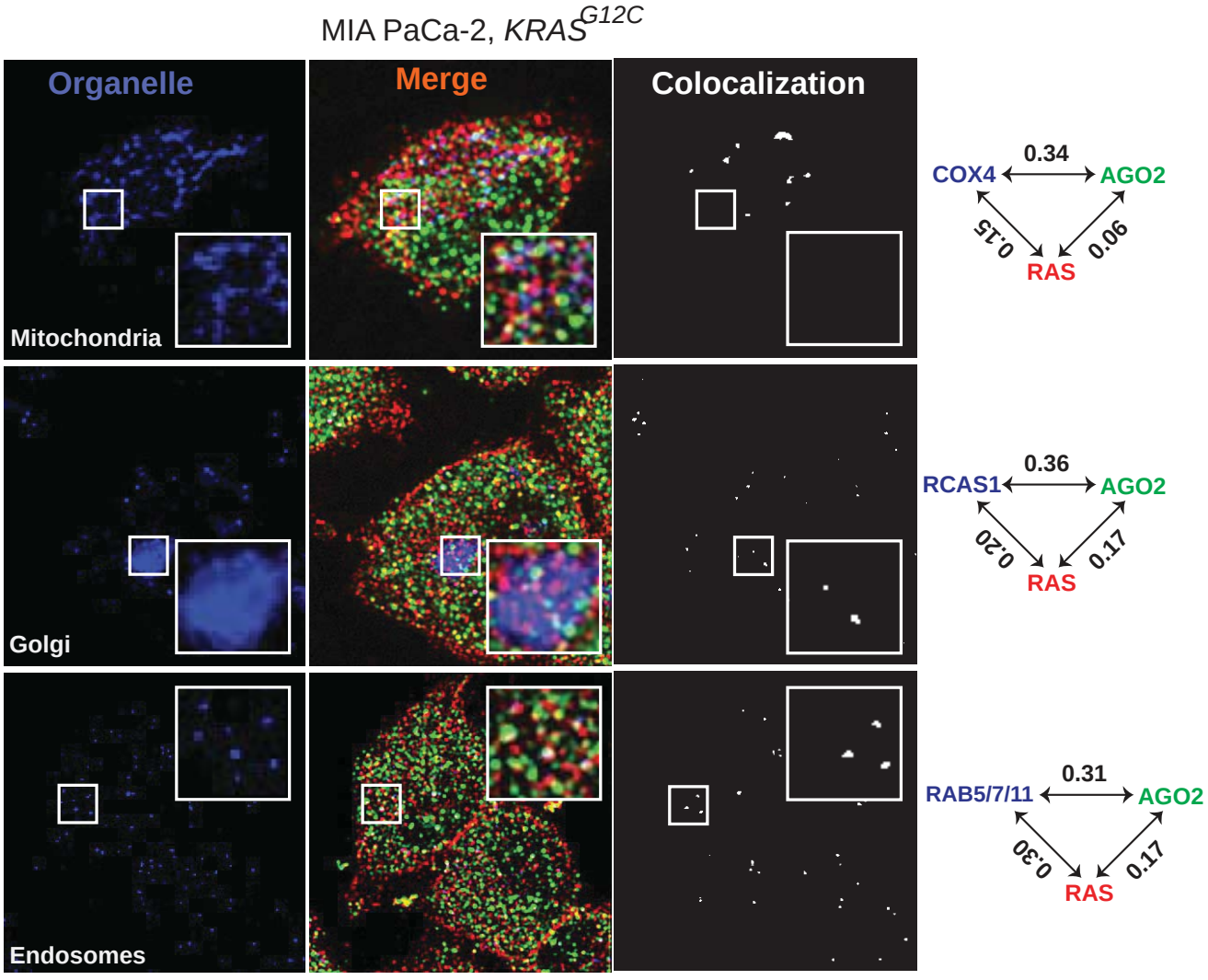

Figure S2. **Related to Figure 2. Specificity of RAS10 mAb and co-localization of RAS and AGO2 in the endoplasmic reticulum** (**A**) Specificity of the RAS10 mAb is demonstrated by pre-incubating the antibody with switch I domain specific (30-39aa) or non-specific (34-43aa) RAS peptides, prior to immunofluorescence analysis. As seen, both the membrane-bound and intracellular staining was abrogated upon pre-incubation of the RAS10 Ab with RAS peptide spanning the RAS10 Ab epitope in the Switch I effector domain (aa 30-39) but not by a RAS peptide spanning the neighboring aa 34-43. (**B**) Pairwise Manders overlap coefficients within 3 randomly selected regions for each organelle. Extent of colocalization within Region I is indicated in Figure 2D. Maximum overlap (marked in yellow) between RAS and AGO2 signals (green/red) is observed in the ER where both proteins are abundantly present. (**C**) Representative images of immunofluorescence analysis of AGO2 (green), RAS (red) and different membrane bound organelles (blue) in MiaPaCa-2 cells. White spots indicate colocalization signals for RAS/AGO2/organelle in each panel. Pairwise Manders overlap coefficients are shown on the right. The inset shows a magnified 6.7 μm x 6.7 μm view of the areas marked. Scale bar, 5 μm.

Figure S3

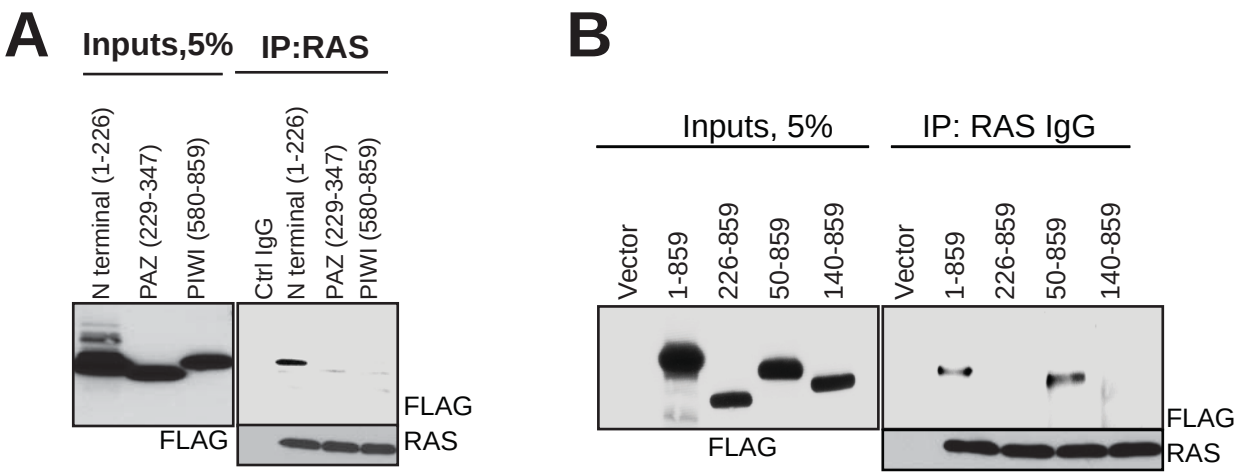

C

```
AGO3 --MEIGSAGPAG------AQPLLMVPRRPGYGTMGKPIKLLANCFQVEIPKIDVYLYEVD 52
AGO4 ----MEALGPGP------PASLFQPPRRPGLGTVGKPIRLLANHFQVQIPKIDVYHYDVD 50
AGO1 --MEAGPSGAAAGAYLPPLQQVFQAPRRPGIGTVGKPIKLLANYFEVDIPKIDVYHYEVD 58
AGO2 MYSGAGPALAPPAPPPPIQGYAFKPPPRPDFGTSGRTIKLQANFFEMDIPKIDIYHYELD 60
          .  .           :  * **. ** *:.*:* ** *:::*****:* *::*
                                                                 59

AGO3 IKPDKCPRRVNREVVDSMVQHFKVTIFGDRRPVYDGKRSLYTANPLPVATTGVDLDVTLP 112
AGO4 IKPEKRPRRVNREVVDTMVRHFKMQIFGDRQPGYDGKRNMYTAHPLPIGRDRVDMEVTLP 110
AGO1 IKPDKCPRRVNREVVEYMVQHFKPQIFGDRKPVYDGKKNIYTVTALPIGNERVDFEVTIP 118
AGO2 IKPEKCPRRVNREIVEHMVQHFKTQIFGDRKPVFDGRKNLYTAMPLPIGRDKVELEVTLP 120
     ***:* *******.*:. **:***  *****:* .***.. :**  . **:.*:::**:*
                74 77     84       94 97 98   104  112 114

AGO3 GEGGKDRPFKVSIKFVSRVSWHLLHEVLTGRTLPEPLELDKPISTNPVHAVDVVLRHLPS 172
AGO4 GEG-KDQTFKVSVQWVSVVSLQLLLEALAG-------HLN-EVPDDSVQALDVITRHLPS 161
AGO1 GEG-KDRIFKVSIKWLAIVSWRMLHEALVSG--------QIPVPLESVQALDVAMRHLAS 169
AGO2 GEG-KDRIFKVSIKWVSCVSLQALHDALSGR--------LPSVPFETIQALDVVMRHLPS 171
     *** **: ****:::::: ** : * :.* .           :. :.::*:**  ***.*
                       137
```

WEDGE DOMAIN:50-139aa

Figure S3. Related to Figure 3. The N-terminal domain of AGO2 is necessary and sufficient to bind RAS. (A) Expression (left panel) and RAS IP interaction analysis (right panel) of FLAG tagged N-terminal, PAZ, or PIWI domains of *AGO2* in HEK293 cells. Immunoblot analysis shows that (1-226aa) N terminal domain is sufficient for RAS interaction using RAS10mAb. **(B)** Expression (left panel) and RAS IP analysis (right panel) of various indicated *AGO2* N terminal deletion constructs in HEK293 cells. Immunoblot analysis indicates that 50-139 aa in the AGO2 N terminal domain is essential for RAS binding. Both RAS IP and IB were performed using RAS10 mAb. **(C)** ClustalW alignment of the Argonaute family proteins spanning the "wedge domain" (50-139 aa, marked in grey). Residues marked in yellow were identified as unique to AGO2 and were mutagenized to alanine for binding analysis. The numbers below indicate the amino acid position. $AGO2^{K98}$ (marked in green) shared with AGO1 was also changed to alanine to be used as control. AGO2 residues K112 and E114, marked in red were critical for RAS interaction.

Figure S4

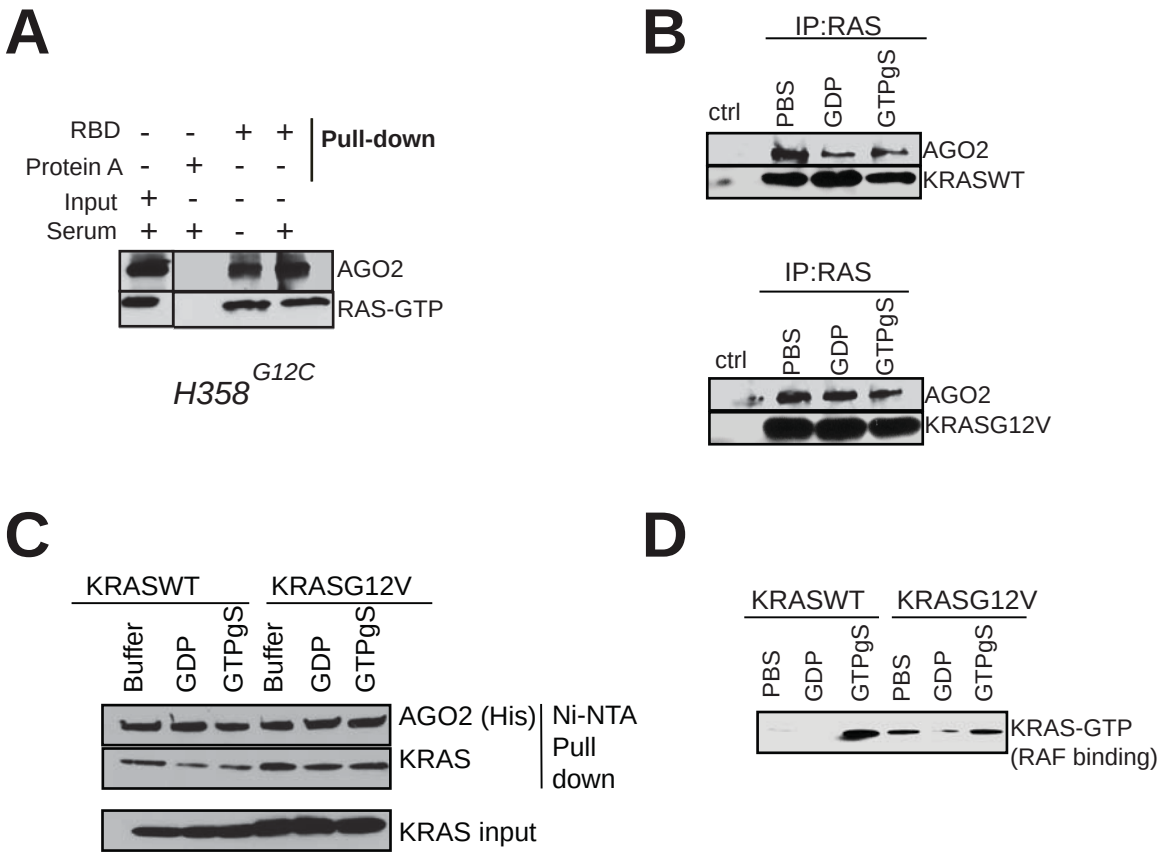
A
RBD - - + +
Protein A - + - -
Input + - - -
Serum + + - +
Pull-down
AGO2
RAS-GTP
H358 G12C
B
IP:RAS
ctrl
PBS
GDP
GTPgS
AGO2
KRASWT
IP:RAS
ctrl
PBS
GDP
GTPgS
AGO2
KRASG12V
C
KRASWT
KRASG12V
Buffer
GDP
GTPgS
Buffer
GDP
GTPgS
AGO2 (His)
KRAS
Ni-NTA Pull down
KRAS input
D
KRASWT
KRASG12V
PBS
GDP
GTPgS
PBS
GDP
GTPgS
KRAS-GTP (RAF binding)

Figure S4. Related to Figure 4. RAS binds AGO2 through its Switch II domain and agnostic to nucleotide bound to RAS (**A**) RBD pull down assay using 1mg of lysates from H358 cells followed by immunoblot analysis for RAS (RAS10) and AGO2 (AGO2, 11A9). (**B**) GDP or GTPγS loading of recombinant KRASWT (top panel) and KRASG12V (bottom panel) proteins prior to RAS-AGO2 *in vitro* co-IP analysis using RAS10 Ab. (**C**) *In vitro* HIS-AGO2 pull down assay after GDP or GTPγS loading of recombinant KRASWT and KRASG12V proteins. (**D**) RBD pull down assay using recombinant KRASWT and KRASG12V proteins loaded with GDP or GTPγS to demonstrate efficiency and specificity of nucleotide loading. Immunoblot analysis for RAS and AGO2 was performed using the RAS10 and AGO2, 11A9 antibodies.

Figure S5

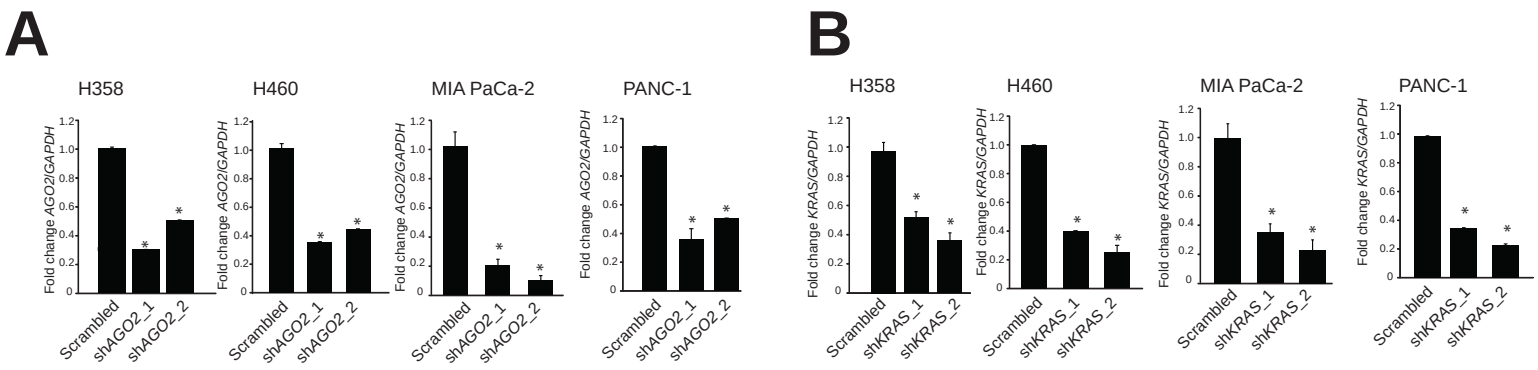

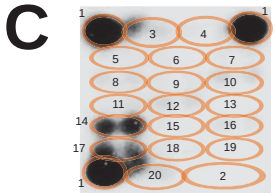

Number	Target	Target Site	Modification
1	Positive Control	N/A	N/A
2	Negative Control	N/A	N/A
3	Erk1/2	Thr202/Tyr204	Phosphorylation
4	Stat1	Tyr701	Phosphorylation
5	Stat3	Tyr705	Phosphorylation
6	Akt	Thr308	Phosphorylation
7	Akt	Ser473	Phosphorylation
8	AMPKα	Thr172	Phosphorylation
9	S6 Ribosomal	Ser235/236	Phosphorylation
10	mTOR	Ser2448	Phosphorylation
11	HSP27	Ser78	Phosphorylation
12	Bad	Ser112	Phosphorylation
13	p70 S6 Kinase	Thr389	Phosphorylation
14	PRAS40	Thr246	Phosphorylation
15	p53	Ser15	Phosphorylation
16	p38	Thr180/Tyr182	Phosphorylation
17	SAPK/JNK	Thr183/Tyr185	Phosphorylation
18	PARP	Asp214	Cleavage
19	Caspase-3	Asp175	Cleavage
20	GSK-3β	Ser9	Phosphorylation

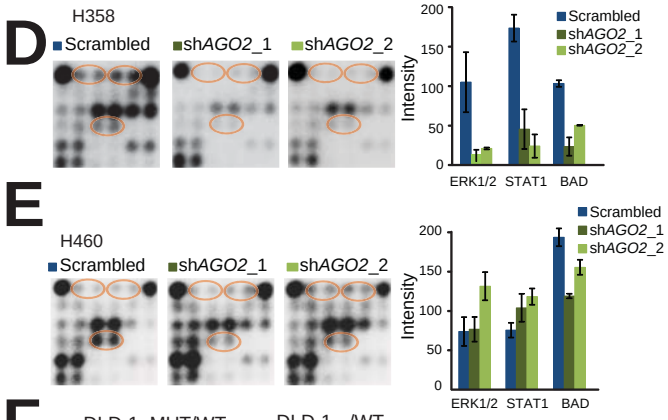

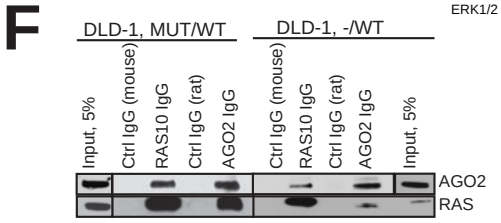

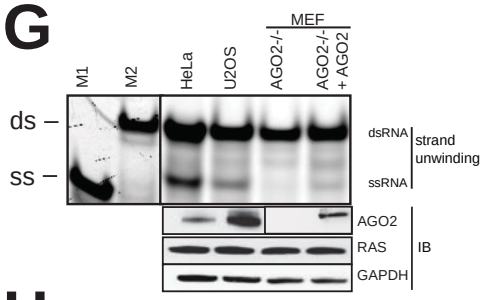

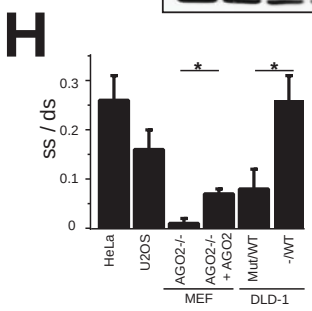

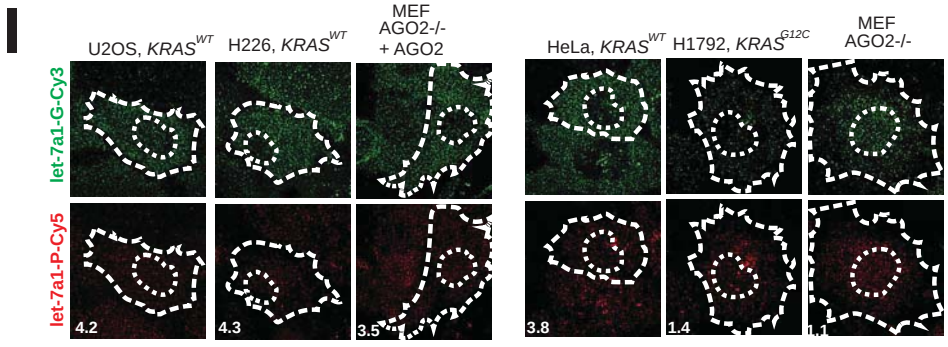

Figure S5. Related to Figure 5. Effects of AGO2 knockdown on RAS signaling and inhibition of AGO2 function in mutant KRAS expressing human cancer cell lines. qRT-PCR of *AGO2* and *KRAS* transcripts demonstrating the efficiency of *AGO2* **(A)** and *KRAS* **(B)** knockdown in the indicated lung and pancreatic cancer cells. Representative assessments are shown. Error bars show standard error of mean and asterisks indicate P values less than 0.05 in each condition. **(C)** Top, representative image of an intracellular signaling array (probed with lysates from NIH3T3 expressing empty vector) used to show the position of target spots of various signaling molecules indicated in the table shown below. Intracellular signaling arrays probed with lysates from *KRAS*-dependent H358 **(D)** and *KRAS*-independent H460 **(E)** lung cancer cells, following knockdown of *AGO2* by two independent shRNAs. Quantification of signal intensities of indicated proteins normalized against control spots, right panel. Parts of these images have been used in Figs. 4d and 4f. (**F**) Co-IP analysis using RAS and AGO2 antibodies show RAS-AGO2 interaction in the DLD-1 isogenic cells expressing $KRAS^{G12C}$ (MUT/WT) or $KRAS^{WT}$ (-/WT). (**G**) Upper panel shows representative images of native acrylamide gel electrophoretic analysis of *let-7* microRNA unwinding in the indicated cellular extracts. M1 and M2 represent double (ds) and single stranded (ss) markers respectively. ($n = 2$, $*p < 0.05$) and shared with Figure 7B in the same electrophoretic run. Lower panel shows immunoblot analysis of the indicated proteins. (**H**) Quantitation of the gel electrophoretic analysis of *let-7* unwinding within different protein extracts. (**I**) Representative Images of the guide strand (green) and passenger strand (red) of *let-7* microRNA in the indicated cell lines, 30 mins post injection. Numbers in the boxes indicate Guide: passenger strand ratio. Scale bar, 10 μm.

Figure S6

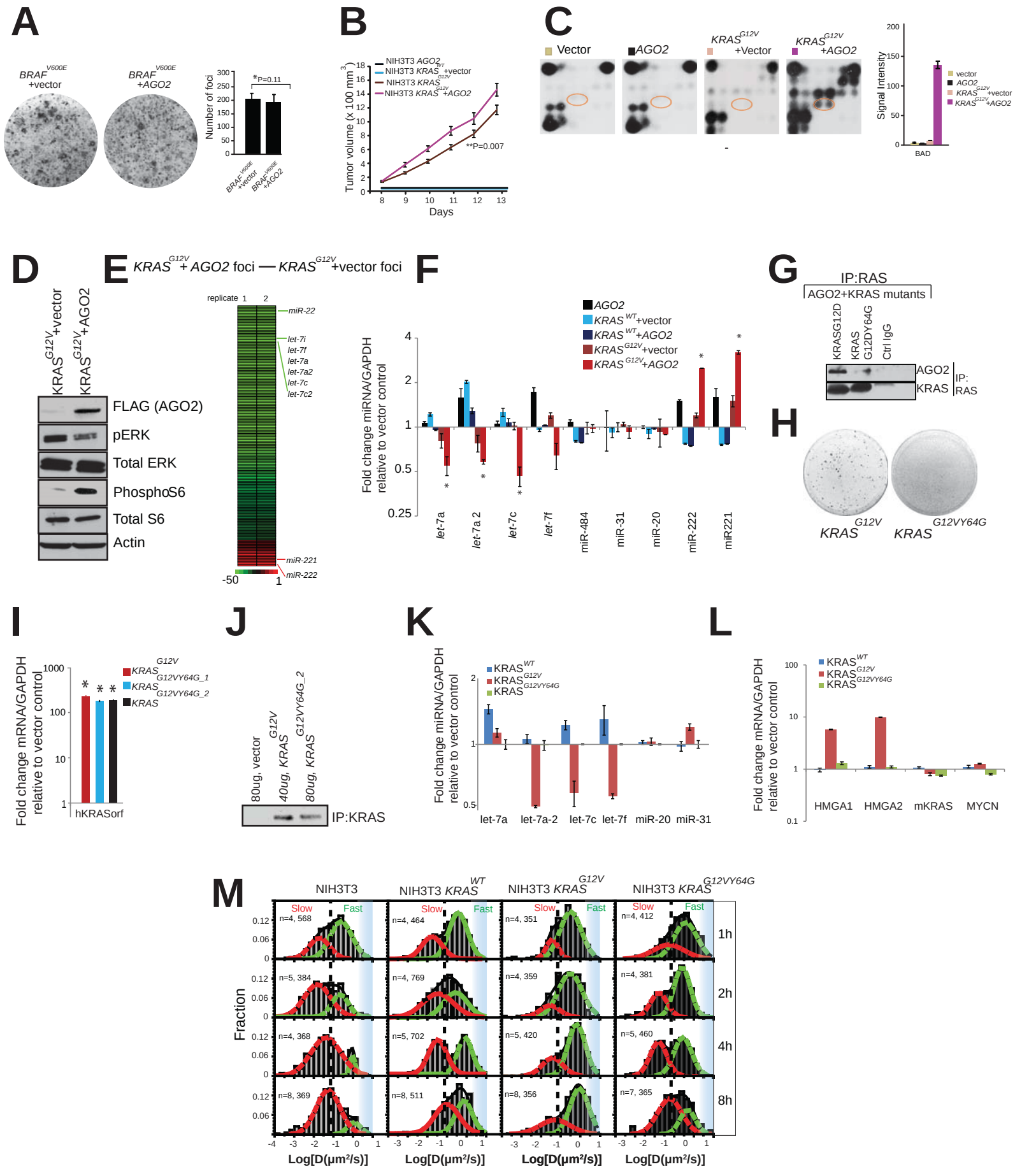
A
BRAF V600E +vector
BRAF V600E +AGO2
Number of foci
*P=0.11
B
NIH3T3 AGO2 WT
NIH3T3 KRAS G12V +vector
NIH3T3 KRAS G12V +AGO2
Tumor volume (x 100 mm3)
**P=0.007
Days
C
Vector
AGO2
KRAS G12V +Vector
KRAS G12V +AGO2
Signal Intensity
vector
AGO2 G12V
KRAS G12V +vector
KRAS G12V +AGO2
BAD
D
KRAS G12V +vector
KRAS G12V +AGO2
FLAG (AGO2)
pERK
Total ERK
PhosphoS6
Total S6
Actin
E
KRAS G12V + AGO2 foci — KRAS G12V +vector foci
replicate 1 2
miR-22
let-7i
let-7f
let-7a
let-7a2
let-7c
let-7c2
miR-221
miR-222
-50
1
F
AGO2
KRAS WT +vector
KRAS WT +AGO2
KRAS G12V +vector
KRAS G12V +AGO2
Fold change miRNA/GAPDH relative to vector control
let-7a
let-7a 2
let-7c
let-7f
miR-484
miR-31
miR-20
miR-222
miR221
G
IP:RAS
AGO2+KRAS mutants
KRASG12D
KRAS G12DY64G
Ctrl IgG
AGO2
KRAS
IP: RAS
H
KRAS G12V
KRAS G12VY64G
I
KRAS G12V
KRAS G12VY64G_1
KRAS G12VY64G_2
KRAS
Fold change mRNA/GAPDH relative to vector control
hKRASorf
J
80ug, vector
40ug, KRAS G12V
80ug, KRAS G12VY64G_2
IP:KRAS
K
KRAS WT
KRAS G12V
KRAS G12VY64G
Fold change miRNA/GAPDH relative to vector control
let-7a
let-7a-2
let-7c
let-7f
miR-20
miR-31
L
KRAS WT
KRAS G12V
KRAS G12VY64G
Fold change mRNA/GAPDH relative to vector control
HMGA1
HMGA2
mKRAS
MYCN
M
NIH3T3
NIH3T3 KRAS WT
NIH3T3 KRAS G12V
NIH3T3 KRAS G12VY64G
Slow
Fast
1h
2h
4h
8h
Fraction
Log[D(μm²/s)]

Figure S6. Related to Figure 6. Oncogenic KRAS interacts with AGO2 to inhibit RISC function, a requisite for foci formation in NIH3T3 cells. (**A**) Representative images of foci formation assays using NIH3T3 cells co-transfected with *BRAF*^{V600E} ± *AGO2*. Quantitation of foci from two independent experiments (right). Error bars show standard error of mean of 2 replicates and P value was calculated using two sided t-test. (**B**) *In vivo* growth of NIH3T3 cells stably overexpressing *AGO2*, *KRAS*^{WT}, *KRAS*^{G12V}+vector, or *KRAS*^{G12V}+*AGO2* in nude mice. For each group (n=8), 500,000 cells were injected and average tumor volume (in mm^3) was plotted on y-axis and days after injection on the x-axis. **(C)** Left, Images of the intracellular signaling arrays probed with lysates from NIH3T3 cells stably expressing vector, *AGO2*, or *KRAS*^{G12V}+/- *AGO2*. The colored circles mark duplicate spots corresponding to p-BAD, left panel. Right, Quantification of signal intensities of p-BAD normalized to control spots, right panel. Parts of these images have been used in Fig. 5b**.** (**D**) Immunoblot analysis of signaling molecules in lysates expressing *KRAS*^{G12V}+/- *AGO2* described above. (**E**) High throughput sequencing analysis of mature microRNA expression levels in RNA obtained from NIH3T3 foci upon co-transfection of *KRAS*^{G12V}+*AGO2* compared to *KRAS*^{G12V}+vector. Heat map indicates differences in normalized read counts for individual microRNAs in the two samples performed in duplicate. The green and red colors denote downregulated (214/781) and upregulated (29/781) mature microRNAs, respectively. The colored scale below shows significant differences in normalized read counts of mature microRNA expression. (**F**) qRT-PCR analysis of *let-7* and the *miR-221/miR-222* family of microRNAs from NIH3T3 cells expressing *AGO2* or KRAS constructs (*KRAS*^{WT} or *KRAS*^{G12V}) alongwith vector or *AGO2*, obtained from the foci assay. U6 RNA was used as a control to normalize the data and vector transfected cells were used as reference. Error bars show standard error of the mean of 4 replicates and asterisks indicate significant log2 fold changes (two sided t-test, P-value less than 0.05) between the indicated conditions compared to vector control. (**G**) *In vitro* co-IP analysis of KRAS-AGO2 interaction with recombinant KRASG12D and KRASG12DY64G proteins, using RAS10 Ab. (**H**) Lack of foci formation of an independent construct encoding *KRAS*^{G12VY64G}. (**I**) qRT-PCR analysis of human KRAS orf transcripts stably expressed in NIH3T3 cells, by plasmids encoding *KRAS*^{G12V} or two independent clones of *KRAS*^{G12VY64G}. (**J**) Immunoprecipitation (IP:KRAS antibody, sc-521) followed by immunoblot analysis (IB: RAS10) of polyclonal populations of NIH3T3 cells stably expressing an independent construct encoding *KRAS*^{G12VY64G}. The amount of total lysate used for IP-IB analysis is indicated in the blot. qPCR analysis of *let-7* family microRNAs (**K**) and *let-7* microRNA targets (**L**) from NIH3T3 cells stably expressing *KRAS*^{WT}, *KRAS*^{G12V} or *KRAS*^{G12VY64G} constructs. U6 RNA and GAPDH mRNA were used as controls to normalize the microRNA and mRNA data respectively and vector transfected cells were used as reference. Target genes *HMGA1/2*, *KRAS* and *MYCN* are known to be regulated by *let-7* microRNA. Error bars show standard error of the mean of 4 replicates and asterisks indicate significant log2 fold changes (two sided t-test, P-value less than 0.05) between the indicated conditions compared to vector control. (**M**) Distribution of *let-7a-1*–Cy5 diffusion coefficients at different time points following microinjection in parental NIH3T3, NIH3T3^{WT} NIH3T3-*KRAS*^{G12V} and NIH3T3-*KRAS*^{G12V,Y64G} cells, as described earlier (Pitchiaya et al., 2012). The fast (green) and slow (red) diffusing particles (demarcated by the dotted lines to guide the eye) were defined based on segregation of the two Gaussian distributions 2h after microinjection. Blue shaded region represents the diffusion coefficients lost due to limited time resolution of tracking. Number of particles analyzed is mentioned within each histogram.

Figure S7

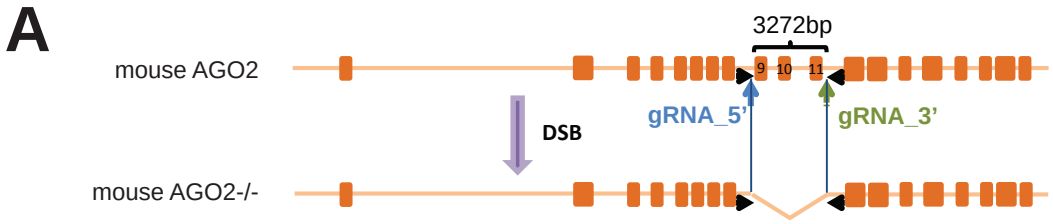
A
3272bp
mouse AGO2
9
10
11
gRNA_5'
gRNA_3'
DSB
mouse AGO2-/-

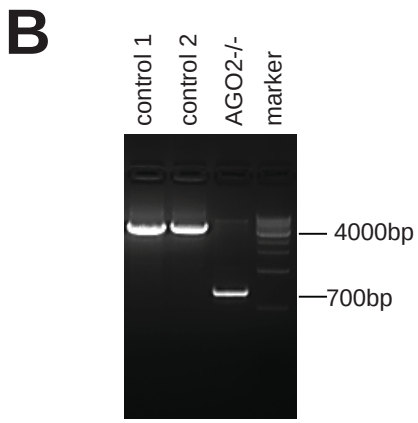
B
control 1
control 2
AGO2-/-
marker
4000bp
700bp

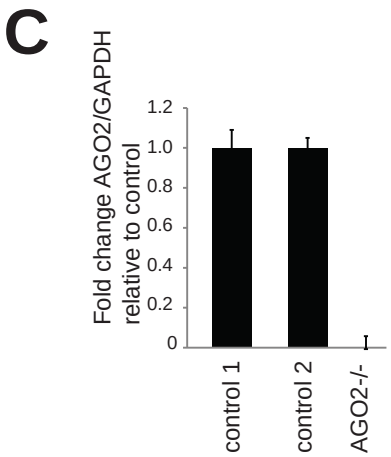
C
Fold change AGO2/GAPDH relative to control
1.2
1.0
0.8
0.6
0.4
0.2
0
control 1
control 2
AGO2-/-

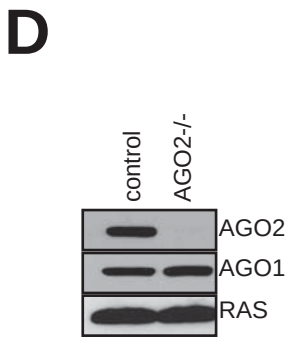
D
control
AGO2-/-
AGO2
AGO1
RAS

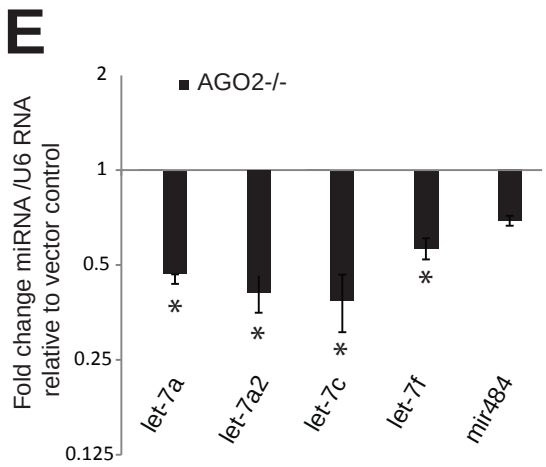
E
AGO2-/-
Fold change miRNA /U6 RNA relative to vector control
2
1
0.5
0.25
0.125
let-7a
let-7a2
let-7c
let-7f
mir484

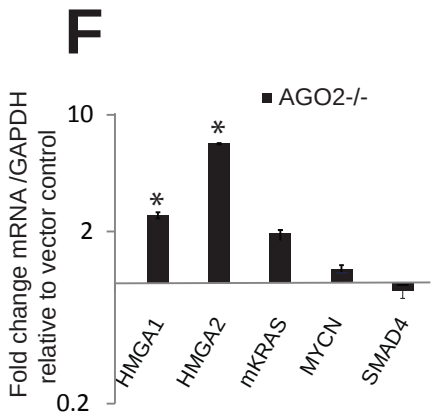
F
AGO2-/-
Fold change mRNA /GAPDH relative to vector control
10
2
0.2
HMGA1
HMGA2
mKRAS
MYCN
SMAD4

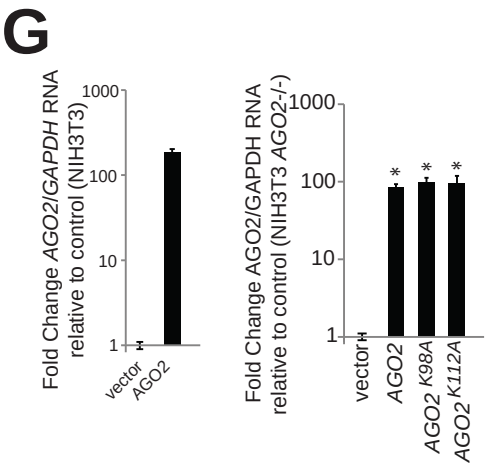
G
Fold Change AGO2/GAPDH RNA relative to control (NIH3T3)
1000
100
10
1
vector
AGO2
Fold Change AGO2/GAPDH RNA relative to control (NIH3T3 AGO2-/-)
1000
100
10
1
vector
AGO2
AGO2 K98A
AGO2 K112A

Figure S7. Related to Figure 7. Generation and characterization of NIH3T3 *AGO2-/-* cells. **(A)** Schematic showing the use of the CRISPR/Cas9 methodology to knockout *AGO2* in NIH3T3 cells. Validation of *AGO2* knockout was performed using genomic PCR **(B)**, RT-qPCR **(C)**, and immunoblot analysis **(D)**. qPCR analysis of *let-7* family microRNAs **(E)** and their target genes **(F)** in NIH3T3 *AGO2*-/- cells. Both the microRNA and transcript levels were compared to NIH3T3 cells treated with vector with no guide RNA. Error bars show standard error of the mean of 4 technical replicates and asterisks indicate significant log2 fold changes (two sided t-test, P-value less than 0.05) between the indicated conditions. **(G)** qPCR analysis of *AGO2* transcripts in NIH3T3 (left) and NIH3T3 *AGO2*-/- (right) cells two days after transfection for foci formation assay, demonstrating similar levels of expression of *AGO2* constructs. Error bars show standard error of the mean of 3 technical replicates and asterisks indicate significant log10 fold changes (two sided t-test, P-value less than 0.005) in *AGO2* expression over that of the vector control.

Table S1. Related to Figure 1

Number	Cell Line	Source	Tissue	Type	*KRAS* or *AGO2* status	RAS co-IP Mass Spec	RAS co-IP Western
1	A549	Human	Lung	Cancer	*KRAS* G12S	X	ND
2	H2009	Human	Lung	Cancer	*KRAS* G12A	ND	X
3	H358	Human	Lung	Cancer	*KRAS* G12C	X	X
4	H441	Human	Lung	Cancer	*KRAS* G12V	X	ND
5	H460	Human	Lung	Cancer	*KRAS* Q61H	ND	X
6	H727	Human	Lung	Cancer	*KRAS* G12V	X	X
7	BXPC3	Human	Pancreas	Cancer	*KRAS* WT	X	X
8	CAPAN-1	Human	Pancreas	Cancer	*KRAS* G12V	X	ND
9	MIA PaCa-2	Human	Pancreas	Cancer	*KRAS* G12C	X	X
10	PANC-1	Human	Pancreas	Cancer	*KRAS* G12D	X	ND
11	PDX 1319	Human	Pancreas	Cancer	*KRAS* G12D	X	ND
12	PL-45	Human	Pancreas	Cancer	*KRAS* G12D	X	ND
13	HPNE	Human	Pancreas	Benign	*KRAS* WT	ND	X
14	DLD-1 (MUT/WT)	Human	Colorectal	Cancer	G13D	ND	X
15	DLD-1 (-/WT)	Human	Colorectal	Benign	WT	ND	X
16	H1792	Human	Lung	Cancer	G12C	ND	ND
17	H226	Human	Lung	Cancer	WT	ND	ND
18	HEK293FT	Human	Embryonic kidney	Benign	for transient overexpression as indicated	ND	X
19	MEF,parental	Mouse	Embryonic fibroblast	Benign		ND	X
20	*AGO2* MEF-/-	Mouse	Embryonic fibroblast	Benign	*AGO2* knockout	ND	X
21	*AGO2* MEF-/- +*AGO2*	Mouse	Embryonic fibroblast	Benign	*AGO2* knockout overexpressing	ND	X

Supplemental Table S1. Cell lines used in the study. Cell lines used in this study for RAS co-IP MS and/or RAS co-IP Western blot analysis and other assays, with their associated *KRAS* mutation status. NIH3T3 stable lines were generated using plasmids encoding $KRAS^{WT}$ or $KRAS^{G12V}$ HEK293 cells were used for transfection for assays in the transient mode. PDX 1319 is a pancreatic cancer derived xenograft cell line.

Table S2. Related to Figure 1

		Lung				Pancreas						Mouse fibroblast			
Protein_ID	Protein	A549	H358	H441	H727	BXPC3	Capan-1	MIA PaCa-2	PANC-1	PL45	PDX 1319	NIH3T3 $KRAS^{G12V}$	NIH3T3 $KRAS^{WT}$	Cumulative spectral counts	Number of cancer cell lines
NP_004976/ NP_002515/ NP_005334	KRAS/NRAS/HRAS	20	44	52	112	75	33	23	36	16	33	98	34	556	12
NP_036286	EIF2C2 (AGO2)	16	45	9	18	38	1	14	12	4	9	48	39	237	12
NP_004090	STOM	0	40	16	56	21	3	0	13	3	2	5	6	165	10
NP_001138303	PHB2	0	3	23	0	5	48	0	15	48	4	7	9	162	10
NP_258260	FCHSD1	26	20	0	0	0	13	0	11	13	0	8	11	76	7
NP_057018	NOP58	10	19	31	0	3	4	4	2	4	6	0	0	73	9
NP_001028886	NOP2	10	13	15	0	2	9	0	0	9	2	0	0	50	7
NP_542193	BRI3BP	0	3	3	20	0	3	3	2	3	3	0	0	40	8
NP_005605	RHEB	10	3	9	0	5	0	0	0	0	7	11	0	35	6
NP_055315	HTATSF1	9	29	0	0	0	2	0	2	2	0	0	0	35	5
NP_036473	GTPBP4	6	2	13	0	0	0	8	0	0	1	0	0	24	5
NP_055118	PES1	5	5	9	0	0	0	5	0	0	3	0	0	22	5
NP_078938	NAT10	6	9	1	0	0	2	4	1	2	1	0	0	20	8
NP_001092688	RAD51AP2	5	4	0	0	0	6	0	4	6	0	0	0	20	5

Supplemental Table S2. Summary of shared peptide hits in RAS coIP mass spectrometry in cancer cell lines. Spectral counts of peptides detected in at least 5 of 10 cancer cell lines tested by tandem mass spectrometry of RAS co-immunoprecipitation.

Table S3. Antibodies used for immunoprecipitation and immunoblotting

#	Antibody	Vendor	Catalog Number	Experiments	Validation method/s	Specificity
1	Anti-Ras Clone 10	Millipore	05-516	IP, IB, IF	recombinant protein detection, peptide competition	human and mouse
2	K-Ras-2B Antibody (C-19)	Santa Cruz	sc-521	IP, IB, IF	recombinant protein detection, KRAS siRNA	only human
3	K-Ras monoclonal Ab	Santa Cruz	sc-30	IB	recombinant protein detection	human and mouse
4	RAS Y13-259 rat monoclonal	Abcam	ab79973	IP	recombinant protein detection	human
5	AGO2 rabbit pAb	Millipore	07-590	IP, IB	recombinant protein detection	human
6	AGO2 mouse mAb, clone 2E12-1C9	Sigma	WH0027161M1	IP, IB, IF	recombinant protein detection	human and mouse
7	AGO2, 11A9	Sigma	SAB4200085	IP, IB, IF	recombinant protein detection	only human
8	Anti-Flag	Sigma	F1804	IB, IP	FLAG-AGO2 detection in HEK 293 cells	NA
9	phospho-Akt S-473	Cell Signaling	4060S	IB	ND	human and mouse
10	phospho-ERK	Cell Signaling	4370	IB	ND	human and mouse
11	SAM68	Santa Cruz	sc-733	IB	ND	human
12	GAPDH-HRP	Cell Signaling	3683	IB	ND	human and mouse
13	Actin	Sigma	A5316	IB	ND	human and mouse
14	Normal rat IgG	Abcam	ab18450	control IP	ND	rat
15	Normal mouse IgG	Millipore	12-371	control IP	ND	mouse
16	Normal rabbit IgG	Millipore	12-370	control IP	ND	rabbit

Supplemental Table S3. Antibodies used in this study. IB: Immunoblotting, IP:Immunoprecipitation, IF: Immunoflourescence

Table S4

Source	Gene	Primer sequence (5'- 3')
Human	AGO2_F	ACCCACCCCACCGAGTTCGAC
Human	AGO2_R	AGTGCGAAGGCCTGCTTGTCC
Human	GAPDH-F	TGTAGTTGAGGTCAATGAAGGG
Human	GAPDH-R	GAGTCCTTCCACGATACCAAAG
Human	AGO2_orf_F	GCACTATCACGTCCTCTGGG
Human	AGO2_orf_R	GGTGTGACACAGCTGGTAGG
Human	KRAS_orf_F	ACACAAAACAGGCTCAGGACT
Human	KRAS_orf_R	AGGCATCATCAACACCCTGT
Human	KRAS_F	TCGACACAGCAGGTCAAGAGGAG
Human	KRAS_R	AGAAAGCCCTCCCCAGTCCTCA
Mouse	MYCN	ACAGAACTGATGCGCTGGAAT
Mouse	MYCN	GGCTGAAGCTTACAGTCCCAA
Mouse	HMGA1_F	CCTCTGGACGGTTGTGTTGT
Mouse	HMGA1_R	TGGGGGAGAGAATACAGGCA
Mouse	HMGA2_F	TGTGCCCTCTGACTTCGTTC
Mouse	HMGA2_R	AGCAAGCCGTCCAAGTACAA
Mouse	KRAS_F	GTTAGCTCCAGTGCCCCAAT
Mouse	KRAS_R	ATTCCCTAGGTCAGCGCAAC
Mouse	SMAD4_F	GGGGAGGGATTTTTCCCTTAAT
Mouse	SMAD4_R	CACCTTGCAGAACAGTGAAGC

Supplemental Table S4. PCR primers used in this study. orf:open reading frame

METHODS SUMMARY

Cell lines, specimen collection

Cell lines, outlined in **Supplemental Table S1**, were purchased from the American Type Culture Collection (ATCC). No further testing for Mycoplasma was performed in the lab. PDX1319 cells were obtained through the Xenograft Core, University of Michigan, directed by Dr. Diane Simeone, University of Michigan, Ann Arbor. Cells were grown in specified media supplemented with serum and antibiotics as per ATCC instructions. Cells were routinely checked for mycoplasma and genotyped to ensure authenticity of cells used.

Coimmunoprecipitation and Tandem Mass Spectrometric analysis

Methods used for immunoprecipitation with RAS/control IgG followed by Tandem Mass Spectrometric analysis and database searching are schematically outlined in **Supplemental Figure S1D**. Complete data of the peptides represented in the RAS co-IP mass spectrometric analysis from the different cell lines are provided in **Supplemental Table S5**. Clustal W analysis was performed using the online program, http://www.ebi.ac.uk/Tools/services/web/toolform.ebi?tool=clustalo with peptide sequences obtained from RAS co-IP MS analysis of H358 lung cancer cells.

Immunoprecipitation (IP) and Western blot Analysis

Fresh protein extracts were prepared by lysis of cells in K buffer (10mM Tris HCl, 0.1%, 150mM NaCl, 1% Triton X100 and protease inhibitors). After brief sonication, debris were removed by centrifugation. For IP, 50-400 µg of lysates were pre-cleared with Protein A/G agarose beads (Pierce) for 1 hour and treated overnight at 4^0C with 1-10 µg of isotypic control or specific antibody as indicated. The immune complexes were then precipitated with Protein A/G agarose beads, washed with K buffer and resuspended in sample loading buffer. RAS10 monoclonal antibody immunoprecipitates were routinely washed at 500mM NaCl for increased stringency and a final wash was carried out with buffer containing 150mM NaCl prior to SDS-PAGE analysis. When AGO2 antibodies were used for immunoprecipitation, the immunoprecipitates were washed with 300mM NaCl containing K-buffer. RNase/DNase treatments of lysates as well as addition of commercial RNA (obtained from Clonetech) were performed prior to pre-clearing of lysates followed by IP. After SDS-PAGE separation, proteins were transferred onto nitrocellulose membranes for immunoblot analysis. For IP using FLAG tagged constructs, FLAG M2 agarose beads (Sigma) were used as per manufacturers' protocol. Antibodies used in the study are detailed in **Table S3**.

Cell Fractionation and Sucrose Density Co-sedimentation analysis Cellular fractions into cytosolic, membrane and nuclear compartments were prepared using Proteoextract Subcellular Proteome Extraction Kit (Millipore), according to manufacturers' instructions. Enrichment of the fractions was validated using antibodies as indicated. Sucrose gradient fractionations werefractionation was performed as described earlier (Hock et al., 2007). Briefly, cells were lysed in buffer containing 25 mM Tris–HCl (pH 7.4), 150 mM KCl, 0.5% NP-40, 2 mM EDTA, 1 mM NaF, 0.5 mM dithiothreitol and protease inhibitors (Roche) and centrifuged at 10,000*g* for 10 min at 4°C. For fractionations, gradients from 15% (w/v) to 55% (w/v) sucrose in 150 mM KCl, 25 mM Tris (pH 7.4) and 2 mM EDTA were used. Lysates were separated by centrifugation at 30,000 r.p.m. for 18 h in an SW41 rotor at 4°C. For each lysate 22 fractions of 0.5ml each were collected, 45ul of which was used for immunoblot analysis.

KRAS and *AGO2* plasmid constructs

Full length FH-*AGO2* and mutant $KRAS^{G12V}$ constructs were obtained from Addgene (pIRESneo-FLAG/HA-*AGO2* corrected plasmid 10822, PI:Thomas Tuschl; FLAG-*AGO2* plasmid 21538: PI: Edward Chan and plasmid 12544 PI: Channing Der). Deletion constructs of *AGO2* spanning different domains (indicated in the figures) were subcloned as FLAG-tagged expression plasmids in pDEST40 (Life Technologies) vector backbone. Site directed mutagenesis was performed on *AGO2* encoded plasmid 10822 to obtain the constructs described in **Figure 3C**. Site directed mutagenesis was performed on the $KRAS^{G12V}$ encoding plasmid to obtain wild type *KRAS4B* and $KRAS^{G12VY64G}$ constructs in the pBabe-puro vector. All constructs were sequence verified by Sanger sequencing at the University of Michigan Sequencing core.

Cell transfection

NIH3T3 or HEK293T cells were transfected with the indicated plasmid constructs using Fugene HD (Promega) according to standard protocols.

Recombinant KRAS and AGO2 proteins

Human derived KRASWT and KRASG12V full length coding regions were cloned as HIS-SUMO tagged proteins in a pET21d plasmid backbone described earlier(Weeks et al., 2007). Site directed mutagenesis was used to introduce the specific mutations described in **Figure 4E-D**. Individual recombinant KRAS proteins were transformed into Rosetta cells for bacterial expression. Cells were resuspended from 1L culture in 40ml of Lysis Buffer (25mM HEPES pH 7.5, 200mM NaCl, A/L, 0.1%bME, 44ul Aprotenin and Leupeptin). Ultra-sonicated for 3 min (6 x 30s, with 30s pause in between) and centrifuged at 17,000rpm in SS34 rotor for 45min to get clear cell lysate. 5 mL Ni-NTA resin was pre-equilibrated (wash) with Lysis Buffer. The cleared cell lysate was then added to the Ni-NTA resin and rotated at 4^{O}C for 1 h followed by centrifugation of Ni resin for 3 min at 1000 x g. The resin was washed 5 times with Ni Wash Buffer 1 (25mM HEPES pH 7.5, 200mM NaCl,). Washed Ni-NTA resin was then loaded onto a column and washed using 10 volumes of buffer. Protein was eluted with 25ml total of Ni Elution Buffer 1 (25mM HEPES pH 7.5, 200mM NaCl, 300mM Imidazole), allowed to sit for 10 minutes after the second loading. Quantitation of protein was performed using Nano Drop. SUMO protease in SUMO buffer (25mM HEPES pH 7.5, 150mM NaCl, 1mM DTT) was then added to the eluate, then pour into YM-10 and overnight at 4 C. Protein was then dialysed into 25mM HEPES pH 7.5, 150mM NaCl, 10% Glycerol and stored at -80C before use.

His tagged KRASG12D (1-166aa) and KRASG12DY64G (1-166aa) were provided by Gideon Bollag (Plexxikon Inc.). His-tagged AGO2 was cloned in baculoviral vector and purified using Ni-NTA columns.

***In vitro* co-immunoprecipitation**

One hundred nanograms of baculoviral AGO2 or AGO1 proteins (Sino Biologicals) and 50 nanograms of the indicated KRAS protein, were incubated in the above mentioned K-buffer with the addition of 0.2% BSA. After 2 hours of incubation at 4^{0}C, 1µg of IgG (RAS or control) was added and incubated further for 2 hours. 10ul of Protein A/G agarose beads (50% slurry) equilibrated in K buffer were then added to pull down the immune complexes, washed five times at RT and resolved using SDS-PAGE prior to immunoblot analysis.

His-AGO2 pull down assay

Thirty micrograms of his-AGO2 (made in house) protein was incubated with 600ul of Ni-NTA or Cobalt-NTA beads, 50% slurry (Qiagen) resuspended in Ni-NTA buffer (20 mM Tris-HCl (pH.8), 0.1% beta-mercaptoethanol, 150 mM NaCl,0.5% Triton X-100). Loading performed at 4^{0}C for 1hr. Subsequently the beads were washed using Ni-NTA buffer and incubated with 25 µl of control/His-AGO2 loaded beads with KRAS proteins in Ni-NTA buffer containing 0.2% BSA. Following incubation for 1.5 h at 4 °C and 5 washes were performed at room temperature with rotation for 5 minutes each and centrifugation at 4000 rpm for 2 min. Finally the binding was assessed by immunoblot analysis (using RAS10 and AGO2 11A9 antibodies).

RAS-GTP pull down assay

The RAS-RAF interaction was studied using the RBD agarose beads as per manufacturer's instructions (Millipore). Lysates were prepared upon lysis in MLB (125mM HEPES, pH 7.5, 750mM NaCl, 5% IGEPAL CA-630, 50mM MgCl2, 5mM EDTA). Lysates were sonicated for 10 seconds, centrifuged to remove debris and cleared lysate was used for binding analysis. 5 microliters of the RAF1-RBD-agarose beads were incubated with the indicated clear lysates for 5 minutes and washed two times in MLB prior to immunoblot analysis. The pull down of RAS by RBD agarose beads indicates the presence of active GTP-bound RAS interacting with RAF1.

Immunofluorescence

Cells were fixed in 4% paraformaldehyde, permeablized with PBS containing 0.1% triton-x100 or 0.05% saponin, blocked in PBS containing 2% normal goat serum (with or without saponin) and stained with (1:200 dilution) of primary antibody and (1:400 dilution) of secondary antibody diluted in blocking solution. The following primary antibodies were used: rabbit-anti-PD1 (endoplasmic reticulum marker, CST), rabbit-anti-COXIV (mitochondrial marker, CST), rabbit-anti-RCAS1 (golgi marker, CST), rabbit-anti-Rab5/7/11 (endosomal markers, CST), rat-anti-Ago2 (Sigma), rabbit-anti-Ago2 (Millipore) and mouse-anti-RAS (Millipore). The following secondary antibodies from Jackson Immuno-Research were used: goat-anti-rabbit-Alexa488, goat-anti-rat-Cy3 and goat-anti-mouse-Cy5. Imaging was performed as described (Pitchiaya et al., 2012; Pitchiaya et al., 2013) using a cell-TIRF system based on an Olympus IX81 microscope equipped with a 60x 1.49 NA oil-immersion objective (Olympus), as well as 405

nm (Coherent©, 100 mW at source, ~65 µW for imaging Alexa-405), 488 nm (Coherent©, 100 mW at source, ~38 µW for imaging fluorescein), 532 nm (Coherent©, 100 mW at source, ~8.5 mW for imaging Cy3) and 640 nm (Coherent©, 100 mW at source, 13.5 mW for imaging Cy5) solid-state lasers. A quad-band filter cube consisting of a z405/488/532/640rpc dichroic filter (Chroma) and z405/488/532/640m emission filter (Chroma) was used to filter fluorescence of the appropriate fluorophore from incident light. Emission from individual fluorophores was detected sequentially on an EMCCD camera (Andor Ixon). Image processing was performed in Imaris (surface rendering) and ImageJ (background correction) and colocalization analysis was done in Image J (using the Coloc 2 plugin).

shRNA mediated knockdown and cell proliferation assays

H358, H460, MIA PaCa-2 and Panc-1 cells were treated with two independent shRNAs in viral vectors (validated Mission shRNA lentiviral particles, Sigma) targeting *KRAS* (TRCN0000040149, TRCN0000010369, TRCN0000040149) or *AGO2* (TRCN0000007865 and TRCN0000011203). After 5 days, cells were trypsinized and plated in triplicate at 5,000 cells per well in 24-well plates. For NIH3T3 stable lines, cells expressing the indicated plasmids were plated as mentioned earlier. The plates were incubated at 37 °C with 5% CO2. Cells were counted using Coulter counter at the indicated times.

Colony formation assay

Cells were treated with lentiviral particles expressing *AGO2* shRNA sequences in 6 well dishes. To select stably transfected clones, puromycin at 1 µg/ml was added to the cells two days after transfection and allowed to grow over 10 days. Medium with selection antibiotic was changed every 2 days. Dishes were then stained using crystal violet, washed with water and photographed.

Focus formation assay

Foci formation assays were performed by transfecting/co-transfecting (the indicated constructs) 150,000 early passage NIH3T3 cells in 6 well dishes using Fugene HD (Promega). After two days, cells were trypsinized and plated onto 150 mm dishes containing 4-5% calf serum. The cells were maintained under low serum conditions and medium was refreshed every two days. After 21 days in culture the plates were stained for foci using crystal violet. Foci were also observed under the microscope to see the altered morphology and were counted manually. Three independent experiments were performed for each condition.

Generation of NIH3T3 stable lines

Early passage NIH3T3 mouse fibroblast cells were plated to 70% confluency and the indicated constructs were transfected using Fugene HD (Promega). Cells transfected with $KRAS^{G12V}$, upon selection with puromycin (1 µg/ul), showed distinct transformed morphology and continued to proliferate as clusters of cells (unlike naïve NIH3T3 cells). The $KRAS^{G12V}$ cells continued to grow in the absence of selection antibiotic and were further transfected with either empty vector (pDEST40) or FLAG-*AGO2* constructs. All the above transfected cells were then selected using G418 (200 µg/ml).

Site directed mutagenesis was performed to generate Y64G mutation in the KRASG12V plasmid, Addgene 12544, described earlier. NIH3T3 cells were transfected with this construct, selected using puromycin to generate polyclonal population of cells stably expressing $KRAS^{G12VY64G}$.

Generation of NIH3T3 *AGO2*-/- line

AGO2-knockout NIH3T3 cells were generated by CRISPR-Cas9-mediated genome engineering (Ran et al., 2013). Genomic regions in murine *AGO2* between exons 8 and 9, and between exons 11and 12 were targeted for deletion using primers TCCTTGGTTACCCGATCCTGG and AGAGACTATCTGCAACTATGG, respectively (PAM motif underlined). PCR products were cloned into the BbsI site of pX458 (pSpCas9(BB)-2A-GFP; obtained from the laboratory of Feng Zhang via Addgene (Cambridge, MA; plasmid 48138)) according to the cloning protocol provided by the Zhang lab (http://www.genome-engineering.org). Cells were transfected with the vectors using Lipofectamine 3000 (Life Technologies) according to the manufacturer's instructions. 48 hours post-transfection, GFP-positive cells were FACS sorted as a single cell into 96-well plate. After culturing for 3 weeks, cells are distributed into two 24 well plates followed by PCR-based genotyping using primers mentioned above. A clone showing deletion of the targeted region in *AGO2* was used for further analysis. Single-cell sorted cells obtained after

transfection of the empty pSpCas9(BB)-2A-GFP construct was used as a negative control. NIH3T3 AGO2-/- cells were also transfected with the KRASG12V plasmid construct to generate stable cell lines after puromycin selection.

Xenograft Models

Five week-old male C.B17/SCID mice were procured from a breeding colony at the University of Michigan. Mice were anesthetized using a cocktail of xylazine (80 mg/kg, intraperitoneal) and ketamine (10 mg/kg, intraperitoneal) for chemical restraint. NIH3T3 cells stably expressing *AGO2*, $KRAS^{WT}$, $KRAS^{G12V}$ +vector or $KRAS^{G12V}$ + *AGO2* (0.5 or 1 million cells for each implantation site) were resuspended in 100 µL of 1× PBS with 20% Matrigel (BD Biosciences) and were implanted subcutaneously into flank region on both sides. Eight mice were included in each experimental group. Tumor growth was recorded every two days by using digital calipers, and tumor volumes were calculated using the formula (π/6) (L × W2), where L = length of tumor and W = width. For the Mia PaCa-2 xenograft model, cells were first treated with either scrambled or *AGO2* shRNA overnight. After 2 days of puromycin selection the cells in each group were injected in 8 mice and the progression of tumor growth was monitored over time. To study oncogenic potential of NIH3T3 $KRAS^{G12VY64G}$ and NIH3T3 *AGO2-/-* cells *in vivo*, subcutaneous implantation of cells on both flanks of mice were performed as before (n=5 mice).

Four to five week old female SCID mice were used for all xenograft studies. Based on power calculation (http://www.biomath.info/power/index.htm), we determined that less than 6 mice per group are sufficient to detect significant differences in tumor volumes between two groups. All mouse experiments were done in a blinded fashion with mice being randomly selected for experiments. The person performing the measurements was blinded to the treatment groups. No animals were excluded in any of the xenograft experiments. All experimental procedures involving mice were approved by the University Committee on Use and Care of Animals at the University of Michigan and conform to their relevant regulatory standards.

Quantitative microRNA and mRNA RT-PCR

For the quantitation of microRNA levels in the NIH3T3 cells transfected with indicated constructs (from both the transient foci assays and stable lines), total RNA was prepared using the miRNeasy kit (Qiagen). MicroRNA RT-qPCR was performed according to the manufacturer's instructions (Applied Biosystems). U6 RNA was used as the endogenous control since its Ct values remained consistent. The vector transfected cells were used as reference.

For quantitation of mRNA transcripts, RNA was extracted from the indicated samples and cDNAs were synthesized using SuperScript III System according to the manufacturer's instructions (Invitrogen). Quantitative RT-PCR was conducted using primers detailed in **Table S4** with SYBR Green Master Mix (Applied Biosystems) on the StepOne Real-Time PCR System (Applied Biosystems). Relative mRNA levels of the transcripts were normalized to the expression of the housekeeping gene *GAPDH* and vector transfected cells were used as reference.

iSHiRLoC analyses

RNA oligonucleotides were purchased from Exiqon and IDT, respectively. RNA oligos were obtained with a 5` phosphate and for the let-7-a1 guide strand, with a 3` Cy5 modification. All oligos were HPLC purified by the appropriate vendor. Oligonucleotide sequences are as follows,

let-7-a1 guide: P-UGA GGU AGU AGG UUG UAU AGU U-Cy5

let-7-a1-passenger: P-CUA UAC AAU CUA CUG UCU UUC C

RNA oligos were heat-annealed in a 1:1 ratio in 1x PBS, resulting in duplex RNAs, and were frozen for further use. Cells were cultured in DMEM (GIBCO) supplemented with 10% (v/v) calf serum (CS, Colorado serum) and 1x penicillin-streptomycin (GIBCO) at 37 ^{o}C. Cells (1 - 1.25 x 10^5)were seeded onto delta-T dishes (Bioptechs) 4 days prior to microinjection, such that they were ~80% confluent at the time of microinjection. Regular medium was replaced with a minimal medium (HBS), without serum and vitamins, but containing 20 mM HEPES-KOH pH 7.4, 135 mM NaCl, 5 mM KCl, 1 mM $MgCl_2$, 1.8 mM $CaCl_2$ and 5.6 mM glucose immediately before microinjection. After microinjection, cells were incubated in phenol red-free DMEM containing 2% (v/v) CS in the presence of a 5% CO_2 atmosphere at 37 ^{o}C for the indicated amounts of time prior to imaging.

Microinjection was performed with samples containing 1 µM Cy5 labeled let-7-a1 duplexes and 0.05% (w/v) 10 kDa fluorescein dextran (Invitrogen) in PBS**.** Imaging was performed as described (Pitchiaya et al., 2012; Pitchiaya et al., 2013) using a cell-TIRF system based on an Olympus IX81 microscope equipped with a 60x 1.49 NA oil-immersion objective (Olympus), as well as 488 nm (Coherent©, 100 mW at source, ~38 µW for imaging fluorescein) and 640 nm (Coherent©, 100 mW at source, 13.5 mW for imaging Cy5) solid-state lasers. A quad-band filter cube consisting of a z405/488/561/640rpc dichroic filter (Chroma) and z405/488/561/640m emission filter (Chroma) was used to filter fluorescence of the appropriate fluorophore from incident light. Emission from

individual fluorophores was detected sequentially on an EMCCD camera (Andor Ixon). Particle tracking analysis was performed by using tracks that spanned at least four video frames.

Extract preparation and in vitro miRNA unwinding assay

Cell extracts were prepared as described (Kwak et al, Nat. Struct. Mol. Boil. 2012 and Rakotondrafara et al, Nature protocols, 2011), with minor modifications. Briefly, cells grown in 150 cm^2 flasks (4x per cell line) were trypsinized, diluted with equal volume of FBS containing media and collected by centrifugation at 1500g for 5 min at 4^{o}C. Cells were washed 2 times with cold PBS and resuspended in hypotonic lysis buffer (10mM HEPES-KOH, pH 7.5, 10mM potassium acetate, 0.5 mM magnesium acetate, 0.1 % Igepal, 0.1% Tween-20). Cells were incubated at 4^{o}C for 30 min and the suspension was passed 5-10 x through a 27.5-G needle to promote lysis. The cell extracts were then cleared by centrifuging at 20,000g for 10 min at 4^{o}C and the supernatant were flash frozen and stored at -80^{o}C until use. All buffers contained 1x EDTA-free protease inhibitor cocktail. We typically obtained 15-20 mg/mL protein concentration in the extract. Unwinding assays were performed as described (Nykanen et al, Cell, 2001) with some minor modifications. 10 uL reactions containing 250 fmol double stranded let-7 miRNA (Cy5 labeled at the 3` end of the guide strand and Cy3 labeled in the 3` end of the passenger strand), 75 µg cell extracts, 30 mM HEPES, pH 7.4, 100 mM potassium acetate, 2 mM magnesium acetate, 5 mM DTT. 0.33x protease inhibitor cocktail (Roche), 25 mM creatine phosphate, 1 mM ATP, 0.05 U/uL rRNAsin (Promega) and 0.5 U/uL creatine kinase, were incubated for 10 min at 4^{o}C and 25^{o}C. Then, 2500 fmol of unlabeled guide strand was added to the reaction along with proteinase K (2mg/mL) and the reaction was incubated at 25^{o}C for an additional 10mins. Samples were rapidly transferred to ice, mixed with 2.5 uL of 5x gel loading buffer (50mM Tris.HCl, 0.5% SDS, 0.1% NP40, 50% glycerol) loaded onto 20% TBE gels (10cm x 10cm) and electrophoresed at 200 V for 2.5 h at 4^{o}C. Gels were then scanned using a Typhoon scanner (GE) and bands were quantified using Image J.

Pathscan Intracellular signaling array analysis

Pathscan intracellular signaling arrays were purchased from Cell Signaling. Indicated cells from the overexpression model or after knockdown were serum starved overnight and 40-80 µg of lysates generated from these were applied to the arrays. Arrays were processed according to the manufacturer's instructions and developed using chemiluminescent substrates. For analysis the ImageJ software was used and control spots indicated in **Figure S5C** were used to normalize the data. The quantitative bar charts shown in the study are for those signaling moelcules that show intensity levels of greater than 50 for each of the duplicate spots in a given treatment such as overexpression or knockdown.

microRNA Sequencing

microRNA libraries for sequencing were prepared using the "Illumina® TruSeq® Small RNA Sample Preparation" protocol following the manufacturer's instructions. Briefly, one microgram of total RNA from NIH3T3 foci expressing *KRAS^{G12V}*+vector or *KRAS^{G12V}+AGO2* was sequentially subjected to 3' and 5' RNA adaptor ligations. The adaptor ligated RNA was converted to cDNA using Superscipt II reverse transcriptase and RNA RT primer. The samples are then subjected to 11 cycles of PCR amplification and in the process barcoded. The PCR products were ethanol precipitated and resolved using a 6% TBE PAGE gel, electrophoresed at 145V for 60 minutes. The PCR products observed between 145 and 160 base pairs were excised and passed through a gel breaker tube at 20,000g for 2 minutes. The DNA was eluted from the gel pieces overnight, ethanol precipitated and its size and concentration analyzed by Bio-Analyzer. The barcoded microRNA libraries were sequenced using the Illumina MiSeq sequencing machine.